

# Generating Physically-Consistent Satellite Imagery for Climate Visualizations

Björn Lütjens, Brandon Leshchinskiy, Océane Boulais\*, Farrukh Chishtie\*, Natalia Díaz-Rodríguez\*, Margaux Masson-Forsythe\*, Ana Mata-Payerro\*, Christian Requena-Mesa\*, Aruna Sankaranarayanan\*, Aaron Piña, Yarin Gal, Chedy Raissi, Alexander Lavin, Dava Newman

arXiv:2104.04785v5 [cs.CV] 21 Oct 2024

Deep generative vision models are now able to synthesize realistic-looking satellite imagery. But, the possibility of hallucinations prevents their adoption for risk-sensitive applications, such as generating materials for communicating climate change. To demonstrate this issue, we train a generative adversarial network (pix2pixHD) to create synthetic satellite imagery of future flooding and reforestation events. We find that a pure deep learning-based model can generate photorealistic flood visualizations but hallucinates floods at locations that were not susceptible to flooding. To address this issue, we propose to condition and evaluate generative vision models on segmentation maps of physics-based flood models. We show that our physics-conditioned model outperforms the pure deep learning-based model and a handcrafted baseline. We evaluate the generalization capability of our method to different remote sensing data and different climate-related events (reforestation). We publish our code and dataset which includes the data for a third case study of melting Arctic sea ice and >30,000 labeled HD image triplets – or the equivalent of 5.5 million images at 128x128 pixels – for segmentation guided image-to-image translation in Earth observation. Code and data is available at [github.com/blutjens/eie-earth-public](https://github.com/blutjens/eie-earth-public).

**Index Terms**—Deep Generative Vision Models, Generative AI, Physics-informed Machine Learning, Generative Adversarial Networks, Image to Image Translation, Climate Change, Flooding, Reforestation, Visualization, Synthetic Satellite Imagery, Remote Sensing.

## I. INTRODUCTION

With climate change, natural disasters are becoming more intense [1]. Floods are the most frequent weather-related disaster [2] and already cost the U.S. 4.1 B USD per year [3]; this damage is projected to grow over the next decades [1].

Visualizations of climate impacts are widely used by policy and decision makers to raise environmental awareness and facilitate dialogue on long-term climate adaptation decisions [4]. Visualizations of flood risks, for example, are used in local policy making and community discussion groups as decision-aids

Corresponding author: B. Lütjens; [lutjens@mit.edu](mailto:lutjens@mit.edu). \*indicates equal contribution.

BLü, BLe, AMP and DN are with the Massachusetts Institute of Technology, CRM with Max Planck Institute for Biogeochemistry, FC with The University of British Columbia and Peaceful Society, Science and Innovation Foundation, NDR with University of Granada, OB with Scripps Institute of Oceanography, MMF with Surgical Data Science Collective, AS with MIT CSAIL, AP with US Forest Service, YG with Oxford University, CR with Riot Games, and AL with Pasteur Labs.

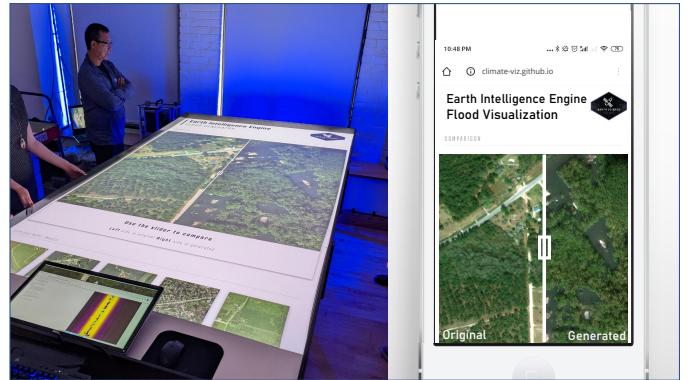


Fig. 1: We synthesize satellite imagery that visualizes flooding (right). We designed the underlying generative vision model to project flooding only in locations that are consistent with a physics-based flood model. The new visualizations could facilitate intuitive and trustworthy communication of climate risks, for example, via tabletop exercises as seen on the left. Explore more results at [climate-viz.github.io](https://climate-viz.github.io).

for flood infrastructure investments [4]. Current visualizations of flood impacts, however, are limited to color-coded flood maps [5], [6], [7] or synthetic street-view imagery [8], [9], which do not convey city-wide flood impacts in a compelling manner, as shown in Fig. 3 and [10]. Our work generates synthetic satellite imagery of future coastal floods that are informed by the projections of expert-validated flood models, as illustrated in Fig. 2. As a geospatial rendering, this imagery might enable a more engaging communication of city-wide flood risks to governmental offices, as demoed in Fig. 1.

We focus on deep generative vision models, such as generative adversarial networks (GANs) [11], as our method for visualization. Generative vision models have generated photorealistic imagery of faces [12], [13], animals [14], [15], street-level flood imagery [9], and satellite observations [16], [17], [18], [19], [20]. Synthetic satellite imagery, however, needs to be explainable [21], [22] and trustworthy [23]. Many complementary approaches exist to increase the trustworthiness of generative vision models, including interpretable networks [24], adversarial robustness [25], [26], [27], or probabilistic predictions with uncertainty [28], [29], [30]. Here, we raise a new question of ‘How can we increase trust in synthetic satellite imagery through physical-consistency?’

We define a synthetic image to be physically-consistent if the depictions in the image are consistent with the output of

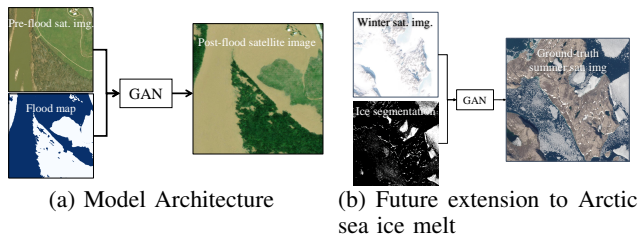


Fig. 2: **Top: Model Architecture.** Our model leverages the semantic image synthesis model, Pix2pixHD [13], and combines a pre-flood satellite image with a physics-based flood map to generate post-flood satellite imagery. **Bottom: Arctic sea ice melt.** We publish a dataset of 19446 labeled image triplets for segmentation guided image-to-image translation which includes an additional case study on melting Arctic sea ice.

a physics-based model, as detailed in Section III-C. Our definition of physical-consistency relates to the field of physics-informed machine learning (ML) in which researchers find novel ways to embed physics domain knowledge into deep learning methods [31], [32], [33], [34], [35]. We considered various physics-informed ML methods to incorporate the physics of floods in a generative vision model as inputs [36], constrained representation [37], [38], [24], training loss [39], hard output constraints [40], [41], [42], or evaluation function [43]. We also considered to embed a generative vision model into a set of physics equations, specifically, in the differential equations of floods as learned parameters [44], [39], dynamics [45], residual [46], [47], differential operator [32], [48], or solution [39]. Finally, we decided to incorporate physics as input and evaluation functions. Specifically, we use a 1-channel flood mask, that represents the projections of a physics-based flood model, and 3-channel satellite imagery as inputs to a deep generative vision model and evaluate the intersection over union (IoU) of the generated image and flood input, as detailed in Section III.

We call our method *Earth Intelligence Engine (EIE)* and associate a novel dataset in segmentation-guided image-to-image translation with it, as detailed in Section III-A. We show that our method outperforms a physics-unconditioned baseline model in Section IV-B and discuss generalization across space, remote sensing instruments, and other climate events (reforestation and Arctic sea ice melt) in Section IV-D.

Our work makes the following contributions:

- A novel framework to measure physical-consistency in synthetic satellite imagery,
- the first physically-consistent and photorealistic visualization of flood risks as satellite imagery,
- an open-source dataset with over 30k labeled high-resolution image-triplets that can be used to study image-to-image translation in Earth observation.

## II. RELATED WORK

We generate physically-consistent visualizations of climate change-related changes in satellite imagery by formulating a



Fig. 3: **Our physically-consistent satellite imagery (c) could enable more engaging and reliable communication of city-scale flood risks [4].** Most existing visualizations of coastal floods or sea-level rise that are aimed towards the public rely on color-coded geospatial rasters (a), that can be unreliable or impersonal [5], [49], [50]. Alternative photorealistic visualizations are often limited to local street-level imagery (b) [8], [9] and lack further spatial context. Images, left-to-right: [5], [5], [8], [8], [51], ours.

semantic image synthesis task and applying deep generative vision models to solve it.

### A. Generative vision modeling.

We formulate the generation of satellite imagery as an image-to-image (im2im) translation problem: learn a mapping from satellite image and segmentation mask to another satellite image [12]. Deep generative vision models have been most successful at solving im2im problems [12]. Generative adversarial networks (GANs) have been successfully used in semantic image synthesis, a subproblem within im2im, to generate photorealistic street scenery from semantic segmentation masks: DCGAN [52], Pix2pixHD [13], DRPAN [13], SPADE [53], or OASIS [54]. Similarly, probabilistic normalizing flows (NFs) [55], [29], variational autoencoders (VAEs) [56], [57], autoregressive models [58], and diffusion-based models ([59] and Fig. A.4) have been adapted to im2im translation. Our use-case requires a deterministic semantic image synthesis model that is capable of generating realistic high-resolution (i.e., 1024x1024px) images. We decided to focus on GANs, because VAEs generate less realistic images ([60], [57] and Fig. 5). NFs could likely capture the distribution of possible images more accurately, but our use-case of engaging visualizations is sufficiently captured with a single deterministic high-resolution image and NFs typically require specialized model architectures that can become computationally expensive. Diffusion-based models show comparable performance to GANs in generating synthetic satellite imagery [61]. However, diffusion-models are currently computationally too expensive to train at 1024x1024px resolution, can still be outperformed by GANs in similar tasks [61], and feature stochasticity that is not needed for this task. So, we decided to extend the high-resolution semantic image synthesis model, pix2pixHD [13], to take in 4-channel images that include physical information and to generate satellite imagery that is both photorealistic and physically-consistent.

### B. Climate change visualization tools

Visualizations of climate change are commonly used in policy making and community discussions on climate adaptation [4], [62]. Landscape or 'street-view' visualizations are used to raise environmental awareness in the general public or policy [10], [9], because they can convey the impacts of

climate change, such as rising sea levels or coastal floods, in a compelling and engaging manner ([10], Fig. 3b). Most landscape visualizations, however, are limited to regional information [8]. Additionally, most landscape visualizations require expensive physics-based renderings and/or high-resolution digital elevation models [8]. Alternative visualization tools of coastal floods or sea-level rise are color-coded maps, such as [63], [5], [50]. Color-coded maps convey the flood extent on a city-wide scale, but are less engaging than a photorealistic image [4]. We are generating compelling visualizations of climate change-related events as satellite imagery to aid in policy and community discussions on climate adaptation.

### III. MATERIALS AND METHODS

To synthesize satellite imagery that depicts floods, we have trained a deep generative vision model. Specifically, we trained a pix2pixHD GAN [13] to translate a *pre-flood* satellite image and a corresponding *flood mask* segmentation map to a *post-flood* satellite image that depicts the flood, as shown in Fig. 2a. The mapping dimensions are:  $[(1024, 1024, 3), (1024, 1024, 1)] \rightarrow (1024, 1024, 3)$ . First, the model is trained and evaluated with flood masks that are derived from the post-flood images via a segmentation model (see Section IV-C) and, then, during inference the model uses flood masks from a physics-based flood model. We train and evaluate the flood visualization and segmentation models on multiple datasets with a total of over 10k HD image-triplets. Our experimental setup evaluates if the model can visualize the precise flood extent as it would be simulated by a flood model – the GAN model is not intended or evaluated to downscale or correct biases inherent in flood models. We discuss an extension to generate imagery of reforestation and towards visualizing Arctic sea ice melt. We describe our datasets in Table I and Section III-A, the model architecture in Section III-B, and we define physical-consistency in Section III-C.

#### A. Data Overview.

As part of this study, we have created nine open-source datasets in flooding, reforestation, and sea ice melt, which are summarized in Table I and detailed in Appendix A. The datasets are formatted as image-triplets for creating an image-to-image (im2im) translation model or as image-pairs for creating a segmentation (seg) model. In total, the data is approximately 90 GB or 32k sets of images.

##### 1) Main flood dataset

In our main dataset, **xbd2xbd**, we have assembled 3284 image-triplets from seven flood events in different regions and time, as detailed in Appendix A. Our method requires a large collection of *post-event* images that depict how climate events impact a landscape. However, these post-event images are usually challenging to acquire. In the case of flooding, obtaining post-flood images that display standing water is hindered by cloud-cover, time of standing flood, satellite revisit rate, atmospheric noise, and cost of high-resolution imagery. For the xbd2xbd dataset, we have sourced it by selecting flood-related data from the xBD xview2 dataset [51]. Here, each post-flood image is already paired with a pre-flood image,

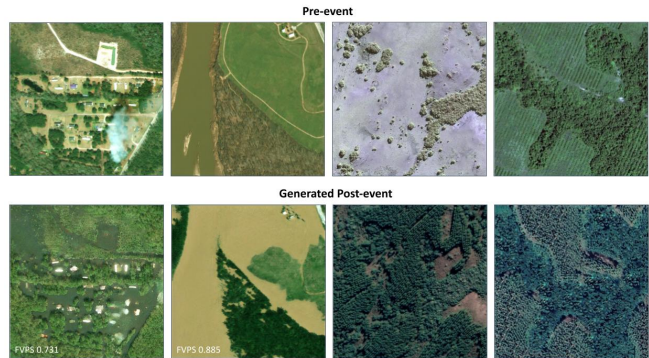


Fig. 4: Our model, titled the *Earth Intelligence Engine*, visualizes how flooding (left) or reforestation (right) would impact the landscape as seen from space.

which was taken by the same satellite constellation over the same region before the flood struck. The pre- and post-flood data have HD  $1024 \times 1024$  px/img resolution with ground-sample distance  $\sim .5$  m/px, are RGB, and were taken by the Maxar DigitalGlobe satellites.

To add the layer of physical consistency, we associate the pre- and post-flood pairs with a binary low- ( $\sim 30$  m/px) or high-resolution ( $\sim .5$  m/px) flood mask. Because flooding hindcasts typically do not exactly match the observed flood extent (see e.g., [64] for hurricane Harvey), we derive the flood mask inputs that are used to train the im2im model from the post-flood images using a separate flood segmentation model. To train this flood segmentation model, we have created the **xbd-seg** dataset which contains 109 pairs of post-flood images and corresponding hand-labelled flood segmentation masks.

##### 2) Auxiliary datasets

After training and evaluating the im2im model on masks of the observed flood extent, we test if it can also visualize predictions from a physics-based flood model using the **xbdfathom** dataset. The xbdfathom dataset pairs the pre-flood images in the xbd2xbd hurricane Harvey validation set with  $\sim 30$  m/px flood masks from the Fathom-US hydraulic model framework hindcast, as detailed in Appendix A-A3. The datasets, **naip2xbd**, **naip2hou**, and **hou-seg**, are used in Section IV-D2 to test if our model could visualize flooding by using NAIP aerial imagery as input, which would be available across the full U.S. East Coast. The datasets, **forest** and **forest-gtm**, are used to study reforestation visualizations in Section IV-D3 and described in Appendix A-B. Finally, we created the **arctic** dataset in A-C, which we did not use in model training, but publish to facilitate extensions of our method for visualizing sea ice melt.

#### B. Model architecture.

The central model of our pipeline is a generative vision model that learns the physically-conditioned image-to-image transformation from pre-flood image to post-flood image. We leveraged the existing implementation of pix2pixHD [13]. Pix2pixHD is a state-of-the-art semantic image synthesis model that uses multi-scale generator and discriminator architectures to generate high-resolution imagery and we refer to the original paper [13] for details on the model architectures.

TABLE I: **Data Overview.** We created nine datasets to study image-to-image (im2im) translation and segmentation (seg) for flood, reforestation, and sea ice melt events. In total, the datasets contain  $\approx 90GB$  or  $32k$  HD image-pairs or -triplets.

Data name	Event	Task	Data sources	test split	# imgs	Size	Description
<b>xbd2xbd</b>	flood	im2im	maxar-xbd -> maxar-xbd	random	3284	9.8 GB	Main dataset with HD image-triplets from 7 floods in different regions and times. Each image-triplet contains a pre-flood and post-flood image and a generated flood mask.
<b>xbd-seg</b>	flood	seg	maxar-xbd	random	109	160 MB	Ground-truth flood segmentation masks for a subset of the imagery in xbd2xbd.
<b>xbdfathom</b>	flood	im2im	maxar-xbd + fathom	inference	108	448 KB	Flood masks from a hindcast of a flood model for hurricane Harvey. Aligned with pre-flood images from the xbd2xbd validation set.
<b>naip2xbd</b>	flood	im2im	naip -> maxar-xbd	held-out sensor (difficult)	2063	6.1 GB	Data to evaluate im2im translation between two sensors with significant internal variance. Here, mapping from NAIP aerial imagery to all Maxar images in the xbd2xbd dataset.
<b>naip2hou</b>	flood	im2im	naip -> maxar-houston	held-out sensor	5602	16 GB	Data to evaluate im2im translation between two sensors. Here, mapping from NAIP aerial imagery to a single swath of a Maxar satellite over West Houston after hurricane Katrina.
<b>hou-seg</b>	flood	seg	maxar-houston	random	260	370 MB	Ground-truth flood segmentation masks for a subset of the imagery in naip2hou.
<b>forest</b>	reforestation	im2im	sen2 -> sen2	random	1272	5.5 GB	Forests before and after reforestation, including ground-truth reforestation masks. Used to evaluate generalization across climate events.
<b>forest-gtm</b>	reforestation	im2im	sen2 -> sen2	held-out region	107	460 MB	Held-out images of reforestation in Guatemala. Used to evaluate generalization in space.
<b>arctic</b>	sea ice melt	im2im	sen2 -> sen2	random	19446	51 GB	Winter and Summer images of coastal areas in the Arctic, including generated sea ice masks. Not used in paper, but included to encourage visualization of the future Arctic.

We extended the input dimensions to  $1024 \times 1024 \times 4$  to incorporate the focus area mask. We experimented with different parameters (see Section C), but eventually decided to use the same architecture and hyperparameters as in [13]. We trained the model from scratch on each dataset. For the xbd2xbd dataset, training took 200 epochs in  $\sim 7$  hrs on  $8 \times V100$  Google Cloud GPUs. The resulting pipeline is modular, such that it can be repurposed for visualizing other climate impacts.

### C. Trust in flood images through physical-consistency.

We define a *physically-consistent* model as one that fulfills laws of physics, such as, conservation of momentum, mass, and energy [33]. For example, most coastal flood models consist of numerical solvers that resolve the conservation equations to generate flood extent predictions [65]. Here, we consider a flood image to be physically-consistent if it depicts the predictions of a physically-consistent model.

Specifically, we define our generated satellite imagery,  $I_G \in \mathcal{I} = [0, 1]^{w \times h \times c}$  with width,  $w = 1024$ , height,  $h = 1024$ , and number of channels,  $c = 3$ , to be physically-consistent if it depicts the same flood extent as the binary flood mask,  $F \in \mathcal{F} = \{0; 1\}^{w \times h}$ . We implemented a flood segmentation model,  $m_{\text{seg}} : \mathcal{I} \rightarrow \mathcal{F}$ , to measure the depicted flood extent in the generated image. If the flood extent of a generated image and the coastal flood model match within a margin, the image is in the set of physically-consistent images, i.e.,  $\mathcal{I}_{\text{phys}} = \{I_G \in \mathcal{I} : \|m_{\text{seg}}(I_G) - F\| < \epsilon\}$ . The generated image is considered photorealistic, if it is contained in the manifold of naturally possible satellite images,  $\mathcal{I}_{\text{photo}} \subset \mathcal{I}$ . Hence, we are looking for a conditional image generation function,  $g$ , that generates an image that is both, physically-consistent and photorealistic, i.e.,  $g : \mathcal{I}_{\text{photo}} \times \mathcal{F} \rightarrow \mathcal{I}_{\text{photo}} \cap \mathcal{I}_{\text{phys}}$ . Here, we condition the GAN on the flood mask,  $F$ , and use a

custom evaluation function to identify the generation function,  $g$ .

## IV. RESULTS

In Section IV-A, we define the evaluation metrics. Section IV-B analyses the physical-consistency and visual quality of the generated flood imagery on the xbd2xbd dataset and Section IV-C evaluates the underlying flood segmentation model. In Section IV-D1, we query the trained im2im model with flood masks from a physics-based flood model for selected locations in Houston, TX. In Section IV-D2, we evaluate which steps would be necessary to generate a flood visualization layer across the full U.S. East Coast. In Section IV-D3 and Section IV-D4, we extend the model to visualize reforestation, and describe a dataset for future extensions towards visualizing Arctic sea ice melting.

### A. Evaluation Metrics.

Evaluating synthetic imagery is difficult [66], [67]. Most evaluation metrics measure photorealism or sample diversity [67], but not physical consistency [68] (see, e.g., SSIM [69], MMD [70], IS [71], MS [72], FID [73], [74], or LPIPS [75]).

To evaluate physical consistency we propose using the intersection over union (IoU) between water in the generated post-flood image and water in the ground-truth flood mask. This method relies on flood masks, but because there are no publicly available flood segmentation models for high-resolution visual satellite imagery, we trained our own model (Section IV-C). This segmentation model created flood masks of the generated and ground-truth post-flood image which allowed us to measure the overlap of water in between both (best IoU is 1, lowest is 0).

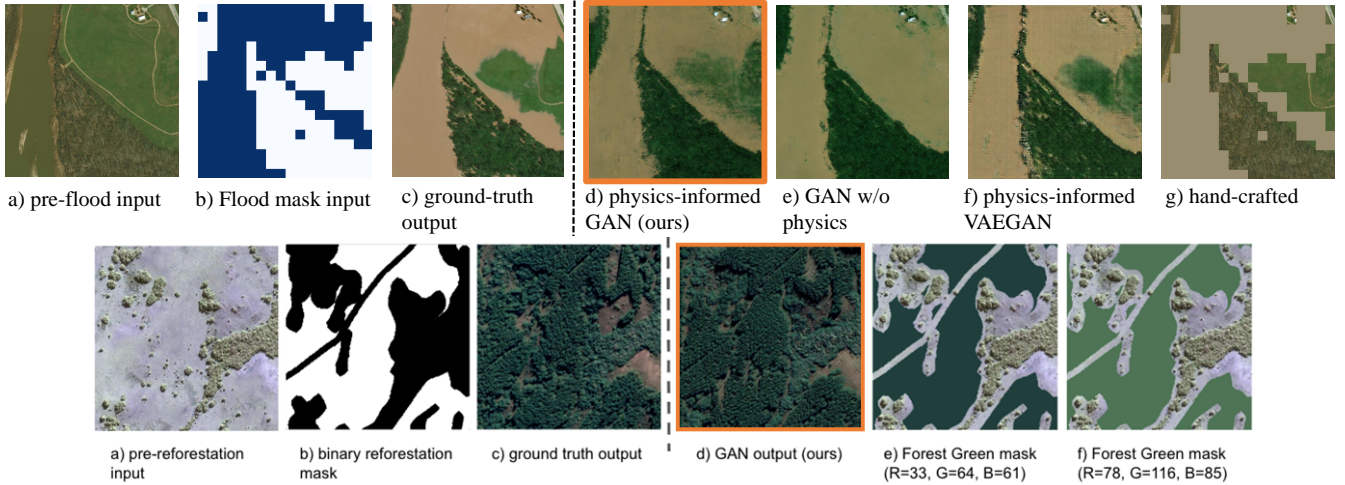


Fig. 5: **Top: Flooding.** The proposed physics-informed GAN (ours, based on [13]) generates post-flood images, (d), from a pre-flood image and flood mask, (a,b). The model outperforms others, (e,f,g), in either physical-consistency or photorealism. The baseline GAN ablates the flood mask and synthesizes a fully-flooded image, (e), rendering the model physically-inconsistent. A VAE-based model [57], creates glitchy imagery, (f), (zoom in). A handcrafted baseline model as used in common visualization tools [50], [63], visualizes the correct flood extent, but is pixelated and lacks photorealism, (g).

**Bottom: Reforestation.** The proposed reforestation mask + pix2pixHD [13] GAN, (d), generates photorealistic reforestation imagery from the inputs, (a,b), outperforming handcrafted baseline models (e,f).

To evaluate photorealism, we used the commonly used perceptual similarity metric Learned Perceptual Image Patch Similarity (LPIPS) [75]. LPIPS computes the feature vectors (of an ImageNet-pretrained AlexNet CNN architecture) of the generated and ground-truth post-flood image and returns the mean-squared error between the two feature vectors (best LPIPS is 0, worst is 1).

Because the joint optimization over two metrics poses a non-trivial hyperparameter optimization problem, we propose to combine the evaluation of physical consistency (IoU) and photorealism (LPIPS) in a new metric (FVPS), called Flood Visualization Plausibility Score (FVPS). The FVPS is the harmonic mean over the submetrics, IoU and  $(1 - \text{LPIPS})$ , that are both  $[0, 1]$ -bounded. Due to the properties of the harmonic mean, the FVPS is 0 if any of the submetrics is 0; the best FVPS is 1. In other words, the FVPS is only 1 if the imagery is both photorealistic and physically-consistent. A small number,  $\epsilon$ , is added for numerical stability.

$$\text{FVPS} = \frac{2}{\frac{1}{\text{IoU} + \epsilon} + \frac{1}{1 - \text{LPIPS} + \epsilon}}. \quad (1)$$

### B. Physical-consistency and photorealism.

We train and evaluate our physics-informed GAN on the xbd2xbd dataset, as detailed in Section III. The dataset contains over 3k HD image-triplets from floods in multiple regions and times. We used all regions during training and evaluated on randomly held-out images of two regions with most visible floods. We evaluate all models on inference with high-res. ( $\sim 0.5$  m/px) and coarse-grained low-res. ( $\sim 30$  m/px) flood masks to imitate flood model predictions at different resolutions. We compare our model against a GAN with the same model architecture, but an ablated flood mask (baseline

GAN) in Section IV-B1, a photoshopped baseline with perfect flood extent in Section IV-B2, and a VAE-based model in Section IV-B3. Overall, we find that our model is on-par with the VAE and outperforms the GAN and photoshopped baseline in terms of physical-consistency or photorealism, respectively.

1) A GAN without physics information generates photorealistic, but non physically-consistent imagery.

The baseline GAN uses the default pix2pixHD [13] with the same architecture and hyperparameters as the physics-informed GAN, but only uses the pre-flood image and not the flood mask as input. The baseline GAN visualized floods at locations where there was no flood according to the flood mask, for example, in Figure 5e-top vs. Fig. 5b-top. In practice, it would be dangerous to operationalize a visualization with false-positive flood predictions. And, the inaccurately modeled flood extent illustrates the importance of measuring physical-consistency, as defined in Section III-C. In our case, we measure physical-consistency via the IoU of the flood masks and, across the high-res. validation set (in Appendix A), the baseline GAN has a lower IoU (0.226) in comparison to the physics-informed GAN (0.502). Despite the photorealism of the baseline GAN (LPIPS = 0.293 vs. 0.265), the physical-inconsistency renders the model non-trustworthy as confirmed by the low FVPS (0.275).

2) A handcrafted baseline model generates physically-consistent but not photorealistic imagery.

Similar to common flood visualization tools [50], the handcrafted model overlays the flood mask input as a hand-picked flood brown (#998d6f) onto the pre-flood image, as shown in Fig. 5g-top. On the low-res. validation set, this model should have a perfect IoU (1) by construction, but our GAN-based flood segmentation model struggles with hard boundaries and measures an acceptable IoU (0.361). Qualitatively, the

handcrafted baseline looks pixelated with flood masks at the resolution of a physical model [5] of 30 m/px and does not account for varying flood color between events (see Fig. 4). The high LPIPS (0.415) indicates quantitatively that the handcrafted visualizations are less photorealistic than the physics-informed GAN (0.283). Despite the lower photorealism, we believe that a handcrafted baseline is a reasonable alternative to generative vision models considering the benefit-cost ratio. In practice, the handcrafted baseline’s main benefit would be the perfect IoU and the GAN’s would be the interpolation of low res. flood masks onto the imagery’s resolution, which can become especially relevant in densely populated areas.

3) *The proposed physics-informed GAN generates physically-consistent and photorealistic imagery.*

To create the physics-informed GAN, we trained a pix2pixHD [13] on the xbd2xbd data, as detailed in Section III and Appendix C. This model successfully learned how to synthesize photorealistic post-flood images from a pre-flood image and a flood mask, as shown in Fig. 4-left. The model improves over all other models either in terms of IoU, LPIPS, or FVPS (Table II). The learned image transformation “in-paints” the flood mask in the correct flood colors and displays an average flood *height* that does not cover structures (e.g., buildings, trees), as shown in 64 randomly sampled test images in Fig. A.3. Occasionally, city-scenes show scratch patterns, e.g., Fig. A.3 (top-left). This could be explained by the unmodeled variance in off-nadir angle, sun inclination, GPS calibration, color calibration, atmospheric noise, dynamic objects (cars), or flood impacts, which is partially addressed in our generalization experiments Section IV-D2. We also train a VAE-based model with GAN components on the same in-/outputs than the physics-informed GAN. Specifically, we use a VAEGAN called BicycleGAN [57], which has the potential to create ensemble forecasts over the unmodeled flood impacts, such as the probability of destroyed buildings. The generated VAEGAN images look smeared Fig. 5f-top and the LPIPS (0.449) is worse than for the physics-informed GAN (0.265) on the high res. validation set.

### C. Flood segmentation model.

Our approach requires a flood segmentation model to generate ground-truth flood masks and evaluate the generated post-flood images, but there does not exist any open-source model that segments floods in high-resolution (<1m/px) satellite imagery. Hence, we labelled our own dataset of 109 HD image-pairs, xbd-seg, and trained a flood segmentation model. Our model is based on pix2pix [12] with a custom loss function and validated with 5-fold cross validation due to the small data size. The model is trained and evaluated at  $\sim 0.5$  m/px and flood masks at  $\sim 30$  m/px are derived via nearest neighbor downsampling of the model outputs. The segmentation model at  $\sim 0.5$  m/px has a mean IoU of 0.343 which matches the expected performance of pix2pix [12] and is sufficient for our task. While one might expect an IoU closer to 1.0, many of our ground-truth flood masks have < 5% of positive labels which skews the IoU towards zero if not perfectly predicted (see, e.g., Fig. D.8-bottom-left). Our segmentation model is detailed in Appendix B and the xbd-seg data in Appendix A-A2.

### D. Generalization performance.

Our project aims to create satellite imagery that visualizes climate phenomena across the globe. So far, however, we have only evaluated our model on one climate phenomenon (floods), one remote sensing instrument (Maxar satellite imagery), a few selected locations, and observation-derived flood masks. To extend our model, we first test if the im2im model can be applied to flood masks from a physics-based flood model.

#### 1) Inference with physics-based flood mask inputs.

We query the physics-informed GAN – trained on xbd2xbd – for the pre-flood imagery from hurricane Harvey and flood masks in xbd2xbd and xbd-fathom. To qualitatively analyse the results, we first plot the predictions (3rd col.) when using the low-res. flood mask inputs (2nd col.) from the xbd2xbd validation dataset, in Appendix D.7. Then, we use the same model and pre-flood image (1st col.), but use the flood masks from the Fathom Global hydraulic model (6th col.) in xbd-fathom as input and plot the predictions in the 5th column.

For both datasets, the generated imagery seems to contain brown-colored floods in areas matching the flood mask inputs. Especially, the images in the 2nd row illustrate the capacity of the im2im model to visualize a different flood extent depending on the input mask. The average IoU across all images in xbd-fathom dataset is 0.398 which is on a similar scale as the IoU on the low-res. xbd2xbd data (0.365) in II. Limitations of the im2im model are visible in forests occasionally being over-painted with a flood brown or houses that appear smeared and are discussed in Appendix D. Overall, these results indicate that the model can generalize from being trained with observation-derived flood masks to being tested with physics-simulated flood masks, assuming that the distribution of pre-flood images is held constant.

#### 2) Generalization across location and remote sensing instruments.

In order to create a visualization layer of flood hazards across the U.S. East Coast, we would need, among others: flood mask inputs across the U.S. East Coast, pre-flood images across the U.S. East Coast, and a model that has been validated for these data streams. We also note that our work only evaluates the im2im model on a tile-by-tile basis and stitching multiple tiles into a seamless large-scale tif entails a set of challenges that are beyond the scope of this work [76], [77].

The flood mask inputs are relatively easy to access, for example, by using a NWS SLOSH National Storm Surge Hazard Map for a hurricane category X storm [5] as discussed in Appendix E. Because this layer is only available at 30m/px, we tested our model’s performance on low-res. flood masks in Section IV-B.

The flood mask inputs at  $\approx 30$  m/px resolution could be accessed for research purposes, for example, from the Fathom Global flood inundation model which was run for multiple climate scenarios [78]. Alternatively, the National Weather Service publishes a 30 m/px National Storm Surge Hazard Map for hurricanes of different categories [5]. As Section IV-D1 showed that 30 m/px physics-based flood masks

TABLE II: **We evaluate photorealism (LPIPS) and physical consistency (IoU)**, to compare our physics-informed GAN with three baselines: a baseline GAN with ablated flood mask; a physics-informed VAEGAN; and a handcrafted baseline. The proposed Flood Visualization Plausibility Score (FVPS) trades-off IoU and LPIPS as a harmonic mean and highlights the performance differences between the GAN with and without physics on low-resolution flood mask inputs. The  $\downarrow$  ( $\uparrow$ ) arrows indicate that a lower (higher) score is better, respectively.

	LPIPS $\downarrow$ high res.	LPIPS $\downarrow$ low res.	IoU $\uparrow$ high res.	IoU $\uparrow$ low res.	FVPS $\uparrow$ high res.	FVPS $\uparrow$ low res.
<b>GAN w/ phys. (ours)</b>	<b>0.265</b>	<b>0.283</b>	<b>0.502</b>	<b>0.365</b>	<b>0.533</b>	<b>0.408</b>
GAN w/o phys.	<b>0.293</b>	<b>0.293</b>	0.226	0.226	0.275	0.275
VAEGAN w/ phys.	0.449	-	<b>0.468</b>	-	0.437	-
Handcrafted baseline	0.399	0.415	<b>0.470</b>	<b>0.361</b>	0.411	<b>0.359</b>

can be used as inputs, we consecutively evaluate if different pre-flood images can be used as inputs.

The pre-flood images in xbd2xbd are from Maxar, which is not freely available across the full U.S. East Coast. Hence, we downloaded pre-flood images from the open-access U.S.-wide mosaic of  $1.0m/px$  visual aerial imagery from the 2019 National Agriculture Imagery Program (NAIP) [79]. For the new dataset, naip2xbd, we pair the pre-flood NAIP images with the post-flood Maxar images and flood masks from xbd2xbd. During the pairing process, we orthorectified the Maxar images to match the NAIP images.

The im2im task from NAIP to Maxar imagery in naip2xbd is significantly more challenging than the Maxar to Maxar task in xbd2xbd, because the learned image-transformation needs to account for the sources of variance in differing remote sensing instruments. These are, for example, resolution, atmospheric noise, color calibration, inclination angle, and other factors. We first applied the physics-informed GAN from xbd2xbd without fine-tuning on the new naip2xbd data, but saw that it generates unintelligible imagery in Fig. A.1-top. After re-training the same model from scratch on the naip2xbd data, the image quality was still relatively poor (not shown). We believe that the variance within the xbd2xbd post-flood images data was too large to learn a mapping from NAIP to Maxar imagery with only 2063 HD images in naip2xbd.

To reduce the learning task complexity, we created the naip2hou dataset, for which we sourced post-flood image tiles from a single open-access Maxar satellite pass over West Houston, TX on 8/31/2017, post-hurricane Harvey [80]. To re-run our pipeline, we labelled an additional 260 flood segmentation masks (hou-seg, taking  $\sim 20$  hrs), retrained the flood segmentation model, and generated flood masks for the naip2hou dataset, as shown in Fig. D.8. The naip2hou dataset contains 5602 HD image-triplets. Then, we re-trained the physics-informed GAN from scratch on the new dataset for 15 epochs in  $\sim 5$  hrs on  $1 \times V100$  GPU. We use a random 80-20 train-val split.

The resulting model for naip2hou has acceptable performance, illustrated in Fig. A.1-top. It does not outperform a handcrafted baseline model in physical-consistency (not shown), but outperforms it in photorealism (LPIPS=0.369 vs. 0.465). This indicates that im2im translation across remote sensing instruments is feasible and a visualization of flood hazards along the U.S. East Coast could be realized in follow-up work.

With xbd2xbd and naip2hou, we created a dataset of a combined 8886 clean image-triplets that we are releasing as the flood-section of our open-source dataset to study segmentation guided image-to-image (im2im) translation in Earth observation. Further, albeit small and geographically biased, the xbd-seg and hou-seg data with a combined 369 HD image-pairs are the first open-source datasets for flood segmentation on visual high-resolution ( $< 1m/px$ ) satellite imagery, to the extent of the authors' knowledge, and will be made available as part of the dataset.

### 3) Generalization across different climate phenomena – visualizing reforestation

Visualizing negative climate impacts such as flooding might evoke anger, fear, or guilt in some viewers. These emotions can encourage pro-environmental behavior [81], [82], [83], but also cause inaction from feeling overwhelmed [84] and hope is needed to maintain environmental engagement [85]. Here we extend the *Earth Intelligence Engine* to visualize the impact of positive hopeful actions, specifically, reforestation. This visualization has already and can be used to encourage policymakers, carbon finance investors [86], [87], or landowners to increase reforestation efforts.

To synthesize satellite imagery of reforested land, the *Earth Intelligence Engine* uses an image of a deforested area along with a binary mask of where trees will be planted as input, as illustrated in Fig. A.2. To train and evaluate the model we collected the **forest** dataset, which contains image-triplets of an RGB pre-reforestation satellite image, a binary reforestation area mask (1=reforestation), and an RGB post-reforestation satellite image. We assembled a total of 1026 train and 246 test high-resolution ( $50cm/px$ )  $1024 \times 1024$  image-triplets via Google Earth Pro (Map data: Google, Maxar Technologies, CNS/Airbus). The dataset spans four different countries: Uruguay, Sierra Leone, Peru, and Mexico, as detailed in Appendix A-B.

We trained the generative vision model that performed best on floods, pix2pixHD, using several augmentation techniques and the default [13] hyperparameters, as detailed in Appendix C-A. We evaluated the model on a random validation split on **forest** and a spatial split testing on 107 held-out images, **forest-gtm**, from Guatemala. We evaluate LPIPS and compare the GAN to a baseline model that applies uniformly colored masks.

Figure 5d)-bottom shows how our model generates photo-realistic visualizations of reforestation projects. The generated

imagery looks more realistic than handcrafted baseline models (e,f), where the reforested area pixels are set to a mean forest color. Our quantitative analysis in Table III confirms that our model outperforms the baselines in both, a random and spatial split. We plot an additional random selection of generated images with their respective inputs in Fig. D.9.

#### 4) Visualizing Arctic sea ice melt

The retreat of the Summer Arctic sea ice extent is one of the most important and imminent consequences of climate change [1]. However, visualizations of melting Arctic sea ice are limited to physics-based renderings, such as [88]. There also does not exist publicly-available daily high-resolution (less than 500m) visual satellite imagery due to satellite revisit rate and cloud cover. To enable the extension of the *Earth Intelligence Engine* for visualizing Arctic sea ice melt, we publish the **arctic** dataset of  $\approx 20k$  image triplets of Winter image, Summer image, and ice segmentation mask, as detailed in Appendix A-C.

## V. DISCUSSION

We proposed a new pipeline to create synthetic and physically-consistent satellite images of future climate events using deep generative vision models. In this section, we discuss limitations and future work.

#### 1) Limitations.

First of all, satellite imagery is currently an internationally trusted source for analyses in deforestation, development, or military domains [89], [90]. With the increased capability of data-generating models, more work is needed in the identification of and the education around misinformation and ethical and trustworthy AI [26], [21]. We point out that our satellite imagery is synthetic, should only be used as a scientific communication aid to better explain our results to decision makers or the general public [4], and we take first steps towards guaranteeing trustworthiness in synthetic satellite imagery.

We had originally envisioned an operational coastal flood visualization across the U.S. East Coast, but discovered that the variance within and between remote sensing instruments is too large to develop an operational visualization as part of a single research paper. Our dataset is not small, as 3-5k HD image-triplets would equal 192-320k triplets at 128x128px resolution. However, our dataset contains spatial and temporal biases including a bias for U.S. areas and vegetation-filled areas. The latter likely contributes to our model rendering human-built structures, such as streets and out-of-distribution skyscrapers in Fig. A.3 top-left, as smeared. Apart from the data limitation, smeared features are still a current concern in state-of-the-art GAN architectures [54] and generative vision model continue to struggle with the sharp lines in remote sensing imagery Fig. A.4. We overcame part of our data limitations by focusing our study on Houston, Tx and using several augmentation techniques, detailed in Appendix C, but this work would likely still benefit from more diverse post-flood images from, e.g., the Maxar or NOAA data archives, or incorporating pre-trained geospatial embeddings [91], [61].

#### 2) Future Work

We envision a tool that can visualize local climate impacts and adaptation techniques at the global scale. By changing the input data, future work can visualize impacts of other well-modeled, visible, and climate-attributed events, including Arctic sea ice melt, hurricanes, wildfires, or droughts. Non-binary climate impacts, such as inundation height, or drought strength could be generated by replacing the binary flood mask with continuous model predictions. Opportunities are abundant for further work in visualizing our changing Earth. This work opens exciting possibilities in generating realistic and physically-consistent imagery with the potential impact of improving climate mitigation and adaptation.

## VI. AUTHOR CONTRIBUTIONS

Conceptualization, B.Lü. and B.Le.; methodology, B.Lü., B.Le., C.R.-M., F.C., N.D.-R., O.B., and A.L.; software, B.Lü. and M.M.-F.; validation, B.Lü., A.P., Y.G., C.R., and D.N.; formal analysis, B.Lü., B.Le., C.R.-M., F.C., N.D.-R., O.B., A.L., and M.M.-F.; investigation, B.Lü. and M.M.-F.; data curation - floods, B.Lü., B.Le., C.R.-M., F.C., N.D.-R., O.B., A.L., and A.M.-P.; data curation - ice, A.S. and B.Lü.; data curation - forest, M.M.-F. and B. Lü.; writing—original draft preparation, B.Lü.; writing—review and editing, B.Lü., B.Le., C.R.-M., F.C., N.D.-R., O.B., A.L., A.S., and M.M.-F.; visualization, B.Lü.; supervision, B.Lü., D.N.; project administration, B.Lü. and B.Le.; funding acquisition, B.Lü., B.Le., D.N. All authors have read and agreed to the published version of the manuscript.

BLü is leading the work and contributed to all sections. BLe started the work. BLe, CRM, FC, NDR, OB, AMP, and AL contributed to the flood experiments in III A-C. AS contributed to the ice experiment. MMF contributed to the reforestation experiment. AP, YG, CR, and DN advised the work.

## VII. FUNDING

This research was sponsored by the United States Air Force Research Laboratory and the United States Air Force Artificial Intelligence Accelerator and was accomplished under Cooperative Agreement Number FA8750-19-2-1000. The views and conclusions contained in this document are those of the authors and should not be interpreted as representing the official policies, either expressed or implied, of the United States Air Force or the U.S. Government. The U.S. Government is authorized to reproduce and distribute reprints for Government purposes notwithstanding any copyright notation herein.

This research was partially conducted at the Frontier Development Lab (FDL), US. For the duration of FDL, the authors gratefully acknowledge support from the MIT Portugal Program, National Aeronautics and Space Administration (NASA), and Google Cloud.

## VIII. DATA AVAILABILITY STATEMENT

The code for this study is available at [github.com/blutjens/eie-earth-public](https://github.com/blutjens/eie-earth-public). The data has been published at [huggingface.co/datasets/blutjens/eie-earth-intelligence-engine](https://huggingface.co/datasets/blutjens/eie-earth-intelligence-engine).



TABLE III: **Reforestation accuracy.** Our model quantitatively outperforms two baseline models that apply a color mask in a random and spatial split.

	LPIPS ↓ random split	LPIPS ↓ spatial split
<b>GAN (ours)</b>	<b>0.503</b>	<b>0.574</b>
Green mask (RGB=33,64,61)	0.794	0.848
Green mask (RGB=78,116,85)	0.845	0.957

## IX. ACKNOWLEDGEMENTS

We are very thankful for Leo Silverberg and Margaret Maynard-Reid for creating the demo at <https://climate-viz.github.io>. We thank Ritwik Gupta for the continuous help in using the xBD dataset, Richard Strange for the help with cloud compute, Prof. Marco Tedesco for advise on the Arctic sea ice, Guy Schumann on flood modeling, Mark Veillette and Cait Crawford for technical direction, and James Parr, Leah Lovgren, Sara Jennings and Jodie Hughes for the organization of FDL and enabling these connections. We greatly appreciate the advise on decision-/policymaking in coastal climate adaptation by Derek Loftis, Sagy Cohen, Capt. John Radovan, Maya Nasr, and Janot Mendler de Suarez. Further, we greatly appreciate the feedback and direction from Esther Wolff, Hannah Munguia-Flores, Peter Morales, Nicholas Mehrle, Prof. Bistra Dilkina, Freddie Kalaitzis, Graham Mackintosh, Michael van Pohle, Gail M. Skofronick-Jackson, Tsengdar Lee, Madhulika Guhathakurta, Julien Cornebise, Maria Molina, Massy Mascaro, Scott Penberthy, John Karcz, Jack Kaye, Mich Lin, Campbell Watson, the FDL research community, and the anonymous reviewers. The authors also gratefully acknowledge support from Earthshot Labs for the reforestation visualization and greatly appreciate the feedback and help from Patrick Leung. We thank Phil Cherner and the members of the Harvard Visualization Research and Teaching Laboratory for co-creating the tabletop visualization platform in Fig. 1, specifically Rus Gant, Kachina Studer, and Michael Quan. The authors declare no conflict of interest.

## REFERENCES

- [1] IPCC, "Global warming of 1.5c. an ipcc special report on the impacts of global warming of 1.5c above pre-industrial levels and related global greenhouse gas emission pathways, in the context of strengthening the global response to the threat of climate change, sustainable development, and efforts to eradicate poverty," 2018. 1, 8
- [2] Centre for Research on the Epidemiology of Disasters (CRED) and UN Office for Disaster Risk Reduction UNISDR, "The human cost of weather-related disasters 1995-2015," 2015. 1
- [3] NOAA National Centers for Environmental Information (NCEI), "U.S. Billion-Dollar Weather and Climate Disasters (2023)," 2023. [Online]. Available: <https://www.ncdc.noaa.gov/billions/> 1
- [4] S. R. Sheppard, *Visualizing Climate Change A Guide to Visual Communication of Climate Change and Developing Local Solutions*. Taylor and Francis Group, March 2012. 1, 2, 3, 8
- [5] NOAA National Weather Service National Hurricane Center Storm Surge Prediction Unit, "National Storm Surge Hazard Maps, Texas to Maine, Category 5," 2020. [Online]. Available: <https://noaa.maps.arcgis.com/apps/MapSeries/index.html?appid=d9ed7904dbec441a9c4dd7b277935fad&entry=1> 1, 2, 3, 6
- [6] Climate Central, "Coastal risk screening tool," 2023, last accessed 04/23. [Online]. Available: <https://coastal.climatecentral.org/> 1
- [7] NOAA, "Sea level rise viewer," 2023, last accessed 04/23. [Online]. Available: <https://coast.noaa.gov/slr/> 1
- [8] B. Strauss, "Surging seas: Sea level rise analysis," 2015. [Online]. Available: <https://sealevel.climatecentral.org/> 1, 2, 3
- [9] V. Schmidt, A. Luccioni, S. K. Mukkavilli, N. Balasooriya, K. Sankaran, J. Chayes, and Y. Bengio, "Visualizing the consequences of climate change using cycle-consistent adversarial networks," *International Conference on Learning Representations (ICLR) Workshop on Tackling Climate Change with AI*, 2019. 1, 2
- [10] S. R. Sheppard, "Landscape visualisation and climate change: the potential for influencing perceptions and behaviour," *Environmental Science and Policy*, vol. 8, no. 6, pp. 637–654, 2005, mitigation and Adaptation Strategies for Climate Change. 1, 2, 3
- [11] I. Goodfellow, J. Pouget-Abadie, M. Mirza, B. Xu, D. Warde-Farley, S. Ozair, A. Courville, and Y. Bengio, "Generative adversarial nets," in *Advances in Neural Information Processing Systems*, vol. 27. Curran Associates, Inc., 2014. 1
- [12] P. Isola, J.-Y. Zhu, T. Zhou, and A. A. Efros, "Image-to-image translation with conditional adversarial networks," in *Computer Vision and Pattern Recognition (CVPR), 2017 IEEE Conference on*, 2017. 1, 2, 6, 14, 15
- [13] T.-C. Wang, M.-Y. Liu, J.-Y. Zhu, A. Tao, J. Kautz, and B. Catanzaro, "High-resolution image synthesis and semantic manipulation with conditional gans," in *Proceedings of the IEEE conference on computer vision and pattern recognition (CVPR)*, 2018, pp. 8798–8807. [Online]. Available: <https://github.com/NVIDIA/pix2pixHD> 1, 2, 3, 4, 5, 6, 7, 14, 15
- [14] J.-Y. Zhu, T. Park, P. Isola, and A. A. Efros, "Unpaired image-to-image translation using cycle-consistent adversarial networks," in *Proceedings of the IEEE International Conference on Computer Vision (ICCV)*, Oct 2017. 1
- [15] A. Brock, J. Donahue, and K. Simonyan, "Large scale gan training for high fidelity natural image synthesis," *arXiv preprint arXiv:1809.11096*, 2018. 1
- [16] C. Requena-Mesa, M. Reichstein, M. Mahecha, B. Kraft, and J. Denzler, "Predicting landscapes from environmental conditions using generative networks," in *German Conference on Pattern Recognition*. Springer, 2019, pp. 203–217. 1
- [17] A. Frühstück, I. Alhashim, and P. Wonka, "Tilegan: Synthesis of large-scale non-homogeneous textures," *ACM Trans. Graph.*, vol. 38, no. 4, Jul. 2019. 1
- [18] T. Mohandoss, A. Kulkarni, D. Northrup, E. Mwebaze, and H. Alemohammad, "Generating synthetic multispectral satellite imagery from sentinel-2," *NeurIPS 2020 Workshop on AI for Earth Sciences*, 2020. 1
- [19] P. Singh and N. Komodakis, "Cloud-gan: Cloud removal for sentinel-2 imagery using a cyclic consistent generative adversarial networks," in *IGARSS 2018 - 2018 IEEE International Geoscience and Remote Sensing Symposium*, 2018, pp. 1772–1775. 1
- [20] N. Audebert, B. Le Saux, and S. Lefevre, "Generative adversarial networks for realistic synthesis of hyperspectral samples," in *IGARSS 2018 - 2018 IEEE International Geoscience and Remote Sensing Symposium*, 2018, pp. 4359–4362. 1
- [21] A. Barredo Arrieta, N. Díaz-Rodríguez, J. Del Ser, A. Bennetot, S. Tabik, A. Barbado, S. Garcia, S. Gil-Lopez, D. Molina, R. Benjamins, R. Chatila, and F. Herrera, "Explainable artificial intelligence (XAI): Concepts, taxonomies, opportunities and challenges toward responsible ai," *Information Fusion*, vol. 58, pp. 82 – 115, 2020. 1, 8
- [22] S. Ali, T. Abuhmed, S. El-Sappagh, K. Muhammad, J. M. Alonso-Moral, R. Confalonieri, R. Guidotti, J. Del Ser, N. Díaz-Rodríguez, and F. Herrera, "Explainable artificial intelligence (xai): What we know and what is left to attain trustworthy artificial intelligence," *Information Fusion*, vol. 99, p. 101805, 2023. 1
- [23] N. Díaz-Rodríguez, J. Del Ser, M. Coeckelbergh, M. L. de Prado, E. Herrera-Viedma, and F. Herrera, "Connecting the dots in trustworthy artificial intelligence: From ai principles, ethics, and key requirements

- to responsible ai systems and regulation,” *Information Fusion*, p. 101896, 2023. 1
- [24] D. Bau, J.-Y. Zhu, H. Strobelt, A. Lapedriz, B. Zhou, and A. Torralba, “Understanding the role of individual units in a deep neural network,” *Proceedings of the National Academy of Sciences*, 2020. 1, 2
- [25] A. Madry, A. Makelov, L. Schmidt, D. Tsipras, and A. Vladu, “Towards deep learning models resistant to adversarial attacks,” in *International Conference on Learning Representations (ICLR)*, 2018. 1
- [26] S. Santamaria, D. Dao, B. Lütjens, and C. Zhang, “Truebranch: Metric learning-based verification of forest conservation projects,” in *ICLR 2020 Workshop on Tackling Climate Change with Machine Learning*, 2020. 1, 8
- [27] B. Lütjens, M. Everett, and J. P. How, “Certified Adversarial Robustness for Deep Reinforcement Learning,” *2019 Conference on Robot Learning (CoRL)*, 2019. 1
- [28] A. E. R. Tilmann Gneiting, “Weather forecasting with ensemble methods,” *Science*, vol. 310, pp. 248–249, 2005. 1
- [29] A. Lugmayr, M. Danelljan, L. Van Gool, and R. Timofte, “SrfLOW: Learning the super-resolution space with normalizing flow,” in *ECCV*, 2020. 1, 2
- [30] B. Lütjens, M. Everett, and J. P. How, “Safe Reinforcement Learning with Model Uncertainty Estimates,” *International Conference on Robotics and Automation (ICRA)*, 2018, 2018. 1
- [31] G. E. Karniadakis, I. G. Kevrekidis, L. Lu, P. Perdikaris, S. Wang, and L. Yang, “Physics-informed machine learning,” *Nature Reviews Physics*, vol. 3, pp. 422–440, 2021. 2
- [32] M. Raissi, “Deep hidden physics models: Deep learning of nonlinear partial differential equations,” *Journal of Machine Learning Research*, vol. 19, no. 25, pp. 1–24, 2018. 2
- [33] J. N. K. Steven L. Brunton, *Data-Driven Science and Engineering: Machine Learning, Dynamical Systems, and Control*. Cambridge University Press, February 2019. 2, 4
- [34] S. Rasp, M. S. Pritchard, and P. Gentine, “Deep learning to represent subgrid processes in climate models,” *Proceedings of the National Academy of Sciences*, vol. 115, no. 39, pp. 9684–9689, 2018. 2
- [35] B. Lütjens\*, B. Leshchinskiy\*, C. Requena-Mesa\*, F. Chishtie\*, N. Díaz-Rodríguez\*, O. Boulais\*, A. Piña, D. Newman, A. Lavin, Y. Gal, and C. Raissi, “Physics-informed GANs for Coastal Flood Visualization,” *arXiv e-prints*, 2020, \* equal contribution. 2
- [36] M. Reichstein, G. Camps-Valls, B. Stevens, M. Jung, J. Denzler, N. Carvalhais, and Prabhat, “Deep learning and process understanding for data-driven earth system science,” *Nature*, vol. 566, pp. 195 – 204, 2019. 2
- [37] B. Lusch, J. Kutz, and S. Brunton, “Deep learning for universal linear embeddings of nonlinear dynamics,” *Nat. Commun.*, vol. 9, 2018. 2
- [38] S. Greydanus, M. Dzamba, and J. Yosinski, “Hamiltonian neural networks,” in *Advances in Neural Information Processing Systems 32*, H. Wallach, H. Larochelle, A. Beygelzimer, F. d Alché-Buc, E. Fox, and R. Garnett, Eds. Curran Associates, Inc., 2019, pp. 15 379–15 389. 2
- [39] M. Raissi, P. Perdikaris, and G. Karniadakis, “Physics-informed neural networks: A deep learning framework for solving forward and inverse problems involving nonlinear partial differential equations,” *Journal of Computational Physics*, vol. 378, pp. 686 – 707, 2019. 2
- [40] A. T. Mohan, N. Lubbers, D. Livescu, and M. Chertkov, “Embedding hard physical constraints in neural network coarse-graining of 3d turbulence,” *ICLR Workshop on AI for Earth Sciences*, 2020. 2
- [41] P. L. Donti, D. Rolnick, and J. Z. Kolter, “DC3: A learning method for optimization with hard constraints,” in *International Conference on Learning Representations (ICLR)*, 2021. 2
- [42] P. Harder, V. Ramesh, A. Hernandez-Garcia, Q. Yang, P. Sattigeri, D. Szwarcman, C. Watson, and D. Rolnick, “Physics-constrained deep learning for climate downscaling,” 2022. 2
- [43] T. Lesort, M. Seurin, X. Li, N. Díaz-Rodríguez, and D. Filliat, “Deep unsupervised state representation learning with robotic priors: a robustness analysis,” in *2019 International Joint Conference on Neural Networks (IJCNN)*. IEEE, 2019, pp. 1–8. 2
- [44] L. A. Garcia and A. Shigidi, “Using neural networks for parameter estimation in ground water,” *Journal of Hydrology*, vol. 318, no. 1, pp. 215–231, 2006. 2
- [45] T. Q. Chen, Y. Rubanova, J. Bettencourt, and D. K. Duvenaud, “Neural ordinary differential equations,” in *Advances in Neural Information Processing Systems 31*. Curran Associates, Inc., 2018, pp. 6571–6583. 2
- [46] A. Karpatne, W. Watkins, J. Read, and V. Kumar, “Physics-guided Neural Networks (PGNN): An Application in Lake Temperature Modeling,” *arXiv e-prints*, p. arXiv:1710.11431, Oct. 2017. 2
- [47] J. Yuval, P. A. O’Gorman, and C. N. Hill, “Use of neural networks for stable, accurate and physically consistent parameterization of subgrid atmospheric processes with good performance at reduced precision,” *Geophysical Research Letter*, vol. 48, p. e2020GL091363, 2021. 2
- [48] Z. Long, Y. Lu, and B. Dong, “Pde-net 2.0: Learning pdes from data with a numeric-symbolic hybrid deep network,” *Journal of Computational Physics*, vol. 399, p. 108925, 2019. 2
- [49] First Street Foundation, “First street foundation flood model technical methodology document,” 2020. 2
- [50] Climate Central, “Sea level rise, predicted sea level rise impacts on major cities from global warming up to 4c,” 2018. [Online]. Available: [https://earthtime.org/stories/sea\\_level\\_rise](https://earthtime.org/stories/sea_level_rise) 2, 3, 5
- [51] R. Gupta, B. Goodman, N. Patel, R. Hosfelt, S. Sajeew, E. Heim, J. Doshi, K. Lucas, H. Choset, and M. Gaston, “Creating xBD: A Dataset for Assessing Building Damage from Satellite Imagery,” in *Proceedings of the IEEE/CVF Conference on Computer Vision and Pattern Recognition (CVPR) Workshops*, June 2019. 2, 3
- [52] A. Radford, L. Metz, and S. Chintala, “Unsupervised representation learning with deep convolutional generative adversarial networks,” 2016. 2
- [53] T. Park, M.-Y. Liu, T.-C. Wang, and J.-Y. Zhu, “Semantic image synthesis with spatially-adaptive normalization,” in *Proceedings of the IEEE Conference on Computer Vision and Pattern Recognition*, 2019. 2
- [54] E. Schönfeld, V. Sushko, D. Zhang, J. Gall, B. Schiele, and A. Khoreva, “You only need adversarial supervision for semantic image synthesis,” in *International Conference on Learning Representations*, 2021. 2, 8
- [55] D. J. Rezende and S. Mohamed, “Variational inference with normalizing flows,” in *Proceedings of the 32nd International Conference on International Conference on Machine Learning - Volume 37*, ser. ICML’15. JMLR.org, 2015, p. 1530–1538. 2
- [56] D. P. Kingma and M. Welling, “Auto-encoding variational bayes,” *Proceedings of the 2nd International Conference on Learning Representations (ICLR)*, 2014. 2
- [57] J.-Y. Zhu, R. Zhang, D. Pathak, T. Darrell, A. A. Efros, O. Wang, and E. Shechtman, “Toward multimodal image-to-image translation,” in *Advances in Neural Information Processing Systems (NeurIPS) 30*, 2017, pp. 465–476. [Online]. Available: <https://github.com/junyanz/BicycleGAN> 2, 5, 6
- [58] N. Parmar, A. Vaswani, J. Uszkoreit, L. Kaiser, N. Shazeer, A. Ku, and D. Tran, “Image transformer,” in *Proceedings of the 35th International Conference on Machine Learning*, ser. Proceedings of Machine Learning Research, J. Dy and A. Krause, Eds., vol. 80. PMLR, 10–15 Jul 2018, pp. 4055–4064. 2
- [59] C. Saharia, W. Chan, H. Chang, C. A. Lee, J. Ho, T. Salimans, D. J. Fleet, and M. Norouzi, “Palette: Image-to-image diffusion models,” *CoRR*, vol. abs/2111.05826, 2021. 2
- [60] A. Dosovitskiy and T. Brox, “Generating images with perceptual similarity metrics based on deep networks,” in *Advances in Neural Information Processing Systems 29*. Curran Associates, Inc., 2016, pp. 658–666. 2
- [61] P. Wolters, F. Bastani, and A. Kembhavi, “Zooming out on zooming in: Advancing super-resolution for remote sensing,” 2023. 2, 8
- [62] S. J. Cohen, S. Sheppard, A. Shaw, D. Flanders, S. Burch, B. Taylor, D. Hutchinson, A. Cannon, S. Hamilton, B. Burton, and J. Carmichael, “Downscaling and visioning of mountain snow packs and other climate change implications in North Vancouver, British Columbia,” *Mitigation and Adaptation Strategies for Global Change planning, Visualization, Water management*, vol. 17, no. 1, pp. 25–49, jan 2012. 2
- [63] NOAA, “Noaa sea level rise viewer,” 2020. [Online]. Available: <https://coast.noaa.gov/slr/> 3, 5
- [64] O. E. Wing, C. C. Sampson, P. D. Bates, N. Quinn, A. M. Smith, and J. C. Neal, “A flood inundation forecast of hurricane harvey using a continental-scale 2d hydrodynamic model,” *Journal of Hydrology X*, vol. 4, p. 100039, 2019. 3, 12
- [65] C. P. Jeleznianski, J. Chen, and W. A. Shaffer, “Slosh: Sea, lake, and overland surges from hurricanes,” *NOAA Technical Report NWS 48, National Oceanic and Atmospheric Administration, U. S. Department of Commerce*, p. 71, 1992, (Scanning courtesy of NOAA’s NOS’s Coastal Service’s Center). 4
- [66] Q. Xu, G. Huang, Y. Yuan, C. Guo, Y. Sun, F. Wu, and K. Weinberger, “An empirical study on evaluation metrics of generative adversarial networks,” *arXiv preprint arXiv:1806.07755*, 2018. 4
- [67] A. Borji, “Pros and cons of gan evaluation measures,” *Computer Vision and Image Understanding*, vol. 179, pp. 41–65, 2019. 4
- [68] D. Ravi, A. B. Szczotka, S. P. Pereira, and T. Vercauteren, “Adversarial training with cycle consistency for unsupervised super-resolution in

- endomicroscopy,” *Medical image analysis*, vol. 53, pp. 123–131, 2019. 4
- [69] Z. Wang, A. C. Bovik, H. R. Sheikh, and E. P. Simoncelli, “Image quality assessment: from error visibility to structural similarity,” *IEEE transactions on image processing*, vol. 13, no. 4, pp. 600–612, 2004. 4
- [70] W. Bounliphone, E. Belilovsky, M. B. Blaschko, I. Antonoglou, and A. Gretton, “A test of relative similarity for model selection in generative models,” 2016. 4
- [71] T. Salimans, I. Goodfellow, W. Zaremba, V. Cheung, A. Radford, and X. Chen, “Improved techniques for training gans,” in *Advances in neural information processing systems*, 2016, pp. 2234–2242. 4
- [72] C. Tong, L. Yanran, P. J. Athul, B. Yoshua, and L. Wenjie, “Mode regularized generative adversarial networks,” in *International Conference on Learning Representations*, 2017. 4
- [73] M. Heusel, H. Ramsauer, T. Unterthiner, B. Nessler, and S. Hochreiter, “Gans trained by a two time-scale update rule converge to a local nash equilibrium,” in *Advances in neural information processing systems*, 2017, pp. 6626–6637. 4
- [74] S. Zhou, A. Luccioni, G. Cosne, M. S. Bernstein, and Y. Bengio, “Establishing an evaluation metric to quantify climate change image realism,” *Machine Learning: Science and Technology*, vol. 1, no. 2, p. 025005, 2020. 4
- [75] R. Zhang, P. Isola, A. A. Efros, E. Shechtman, and O. Wang, “The unreasonable effectiveness of deep features as a perceptual metric,” in *CVPR*, 2018. 4, 5
- [76] X. Li, R. Feng, X. Guan, H. Shen, and L. Zhang, “Remote sensing image mosaicking: Achievements and challenges,” *IEEE Geoscience and Remote Sensing Magazine*, vol. 7, no. 4, pp. 8–22, 2019. 6
- [77] A. Frühstück, I. Alhashim, and P. Wonka, “Tilegan: synthesis of large-scale non-homogeneous textures,” *ACM Trans. Graph.*, vol. 38, no. 4, jul 2019. [Online]. Available: <https://doi.org/10.1145/3306346.3322993> 6
- [78] O. E. J. Wing, P. D. Bates, N. Quinn *et al.*, “A 30 m global flood inundation model for any climate scenario,” *ESS Open Archive*, October 2023. 6
- [79] USDA-FSA-APFO Aerial Photography Field Office, “National Geospatial Data Asset National Agriculture Imagery Program (NAIP) Imagery,” 2019. [Online]. Available: <http://gis.apfo.usda.gov/arcgis/rest/services/NAIP/7>
- [80] Maxar DigitalGlobe, “Open data program, hurricane harvey, 8/31/2017, tileid: 105001000b95e100.” [Online]. Available: <https://www.maxar.com/open-data/7>
- [81] E. F. Thomas, C. McGarty, and K. I. Mavor, “Transforming “apathy into movement”: the role of prosocial emotions in motivating action for social change,” *Personality and Social Psychology Review*, vol. 13, no. 4, pp. 310–333, 2009. 7
- [82] P. Slovic, M. L. Finucane, E. Peters, and D. G. MacGregor, “Risk as analysis and risk as feelings: Some thoughts about affect, reason, risk, and rationality,” *Risk Analysis*, vol. 24, no. 2, pp. 311–322, 2004. 7
- [83] S. Bamberg and G. Möser, “Twenty years after hines, hungerford, and tomera: A new meta-analysis of psycho-social determinants of pro-environmental behaviour,” *Journal of Environmental Psychology*, vol. 27, no. 1, pp. 14–25, 2007. 7
- [84] S. O’Neill and S. Nicholson-Cole, ““fear won’t do it”: Promoting positive engagement with climate change through visual and iconic representations,” *Science Communication*, vol. 30, no. 3, pp. 355–379, 2009. 7
- [85] M. Ojala, “Hope and climate change: the importance of hope for environmental engagement among young people,” *Environmental Education Research*, vol. 18, no. 5, pp. 625–642, 2012. 7
- [86] G. Reiersen, D. Dao, B. Lütjens, K. Klemmer, K. Amara, A. Steinegger, C. Zhang, and X. Zhu, “Reforestree: A dataset for estimating tropical forest carbon stock with deep learning and aerial imagery,” *Proceedings of the AAAI Conference on Artificial Intelligence*, vol. 36, no. 11, pp. 12 119–12 125, Jun. 2022. 7
- [87] B. Lütjens, L. Liebenwein, and K. Kramer, “Machine learning-based estimation of forest carbon stocks to increase transparency of forest preservation efforts,” in *NeurIPS 2019 Workshop on Tackling Climate Change with Machine Learning*, 2019. 7
- [88] NASA/Goddard Space Flight Center Scientific Visualization Studio, “Annual arctic sea ice minimum 1979-2020 with area graph,” 2020, last accessed March 2021. [Online]. Available: [https://climate.nasa.gov/climate\\_resources/155/video-annual-arctic-sea-ice-minimum-1979-2020-with-area-graph/](https://climate.nasa.gov/climate_resources/155/video-annual-arctic-sea-ice-minimum-1979-2020-with-area-graph/) 8
- [89] M. C. Hansen, P. V. Potapov, R. Moore, M. Hancher, S. A. Turubanova, A. Tyukavina, D. Thau, S. V. Stehman, S. J. Goetz, T. R. Loveland, A. Kommareddy, A. Egorov, L. Chini, C. O. Justice, and J. R. G. Townshend, “High-resolution global maps of 21st-century forest cover change,” *Science*, vol. 342, no. 6160, pp. 850–853, 2013. 8
- [90] K. Anderson, B. Ryan, W. Sonntag, A. Kavvada, and L. Friedl, “Earth observation in service of the 2030 agenda for sustainable development,” *Geo-spatial Information Science*, vol. 20, no. 2, pp. 77–96, 2017. 8
- [91] K. Klemmer, E. Rolf, C. Robinson, L. Mackey, and M. Rußwurm, “Satclip: Global, general-purpose location embeddings with satellite imagery,” 2023. 8
- [92] DigitalGlobe, “Open data for disaster response,” 2020. [Online]. Available: <https://www.digitalglobe.com/ecosystem/open-data> 12
- [93] National Geodetic Survey, “Emergency response imagery,” last accessed 04/23. [Online]. Available: <https://storms.ngs.noaa.gov/> 12
- [94] M. Wehner, “Dataset: Hurricane harvey flood,” September 2019, last accessed 8/2024. [Online]. Available: [https://doi.org/10.11578/Harvey\\_Flood/1561271](https://doi.org/10.11578/Harvey_Flood/1561271) 12
- [95] O. E. J. Wing, P. D. Bates, C. C. Sampson, A. M. Smith, K. A. Johnson, and T. A. Erickson, “Validation of a 30 m resolution flood hazard model of the conterminous united states,” *Water Resources Research*, vol. 53, no. 9, pp. 7968–7986, 2017. 12
- [96] C. C. Sampson, A. M. Smith, P. D. Bates, J. C. Neal, L. Alfieri, and J. E. Freer, “A high-resolution global flood hazard model,” *Water Resources Research*, vol. 51, no. 9, pp. 7358–7381, 2015. 12
- [97] M. Wehner and C. Sampson, “Attributable human-induced changes in the magnitude of flooding in the houston, texas region during hurricane harvey,” *Climatic Change*, vol. 166, no. 1, p. 20, May 2021. [Online]. Available: <https://doi.org/10.1007/s10584-021-03114-z> 12
- [98] U. EA, “What is the updated flood map for surface water? version 2.0.” 2019, last accessed 8/2024. [Online]. Available: [https://assets.publishing.service.gov.uk/government/uploads/system/uploads/attachment\\_data/file/842485/What-is-the-Risk-of-Flooding-from-Surface-Water-Map.pdf](https://assets.publishing.service.gov.uk/government/uploads/system/uploads/attachment_data/file/842485/What-is-the-Risk-of-Flooding-from-Surface-Water-Map.pdf) 12
- [99] P. with Code, “Semantic segmentation on cityscapes test,” last accessed 04/23. [Online]. Available: <https://paperswithcode.com/sota/semantic-segmentation-on-cityscapes> 15
- [100] H. Zhao, J. Shi, X. Qi, X. Wang, and J. Jia, “Pyramid scene parsing network,” in *Proceedings of the IEEE Conference on Computer Vision and Pattern Recognition (CVPR)*, July 2017. 15
- [101] H. Li, P. Xiong, J. An, and L. Wang, “Pyramid attention network for semantic segmentation,” 2018. 15
- [102] L.-C. Chen, Y. Zhu, G. Papandreou, F. Schroff, and H. Adam, “Encoder-decoder with atrous separable convolution for semantic image segmentation,” in *Computer Vision – ECCV 2018: 15th European Conference, Munich, Germany, September 8–14, 2018, Proceedings, Part VII*, 2018, p. 833–851. 15
- [103] K. Klemmer, “Improving neural networks for geospatial applications with geographic context embeddings,” 2022. 15
- [104] A. Lacoste, E. D. Sherwin, H. Kerner, H. Alemohammad, B. Lütjens, J. Irvin, D. Dao, A. Chang, M. Gunturkun, A. Drouin, P. Rodriguez, and D. Vazquez, “Toward foundation models for earth monitoring: Proposal for a climate change benchmark,” 2021. 15
- [105] P. Y. Simard, D. Steinkraus, J. C. Platt *et al.*, “Best practices for convolutional neural networks applied to visual document analysis,” in *Icdar*, vol. 3, no. 2003, 2003. 15
- [106] T. Miyato, T. Kataoka, M. Koyama, and Y. Yoshida, “Spectral normalization for generative adversarial networks,” *2018 International Conference on Learning Representations (ICLR)*, 2018. 15
- [107] A. Buslaev, A. Parinov, E. Khvachchenya, V. I. Iglovikov, and A. A. Kalinin, “Albumentations: fast and flexible image augmentations,” *arXiv e-prints*, 2018. 15
- [108] C. Robinson, L. Hou, K. Malkin, R. Soobitsky, J. Czawlytko, B. Dilkina, and N. Jojic, “Large scale high-resolution land cover mapping with multi-resolution data,” in *Proceedings of the IEEE Conference on Computer Vision and Pattern Recognition (CVPR)*, 2019. 15

## APPENDIX A DATASET

### A. Flood imagery

#### 1) *xbd2xbd image translation data*

The xbd2xbd dataset contains further details:

- The dataset contains imagery from seven flood events from multiple regions and years:
  - Hurricane Harvey (hv) in Texas, US, 2017
  - Hurricane Florence in the Carolinas, US, in 2018 (fl)
  - Hurricane Michael in Mexico Beach, US, in 2018 (mi)
  - Hurricane Matthew in North Carolina, US, in 2016 (ma)
  - Spring flooding in the Midwest, US, in 2019 (mw)
  - Sunda strait tsunami in Indonesia in 2018 (in)
  - South Asian monsoon floods in Nepal in 2017 (ne)
- The dataset contains imagery of hurricanes, a spring flood, a tsunami, and a monsoon.
- 30% of all imagery display standing flood ( $\sim 1370$ ). The imagery of Harvey and Florence display the most standing flood.
- The training set contains imagery from all events.
- The validation set is composed of 216 image-triplets: 108 of each hurricane Harvey and Florence. The validation set excludes imagery from hurricane Michael or Matthew, because the majority of tiles does not display standing flood. The 108 images are picked at random from the total set of images of each event.
- We do not have a held-out test set. Primarily, this is due to the limited data size. But we also did not perform extensive hyperparameter optimization of the pix2pixHD model on the validation set and thus mostly avoid the risk of overfitting on the validation set.

We did not use digital elevation maps (DEMs), because our model is intended as visualization layer of existing flood models. Our model is not intended to correct bias in the flood model forecasts. Thus, the information of low-resolution DEMs should already be contained in the flood model that produces the input flood masks.

More open-source, high-resolution, pre- and post-disaster images can be found in unprocessed format on DigitalGlobe’s Open Data repository [92]. Furthermore, NOAA Emergency Response Imagery publishes high-resolution post-flood aerial imagery at  $0.25 - 1m/px$  resolution [93].

#### 2) *xbd-seg flood segmentation data*

We hand selected 109 post-flood images from all events in the xbd2xbd training set to approximately maintain the distribution in event and percentage of flood extent. We labeled the images with floods that were contained by a convex hull by drawing polygon bounding boxes. We labeled the other imagery that contained objects inside the flood (houses, trees) with the help of the photoshop “select areas of similar color”-tool. We used one annotator per image. The masks are binary thresholded and contain 0 for flood or water bodies, 1 for everything else, and 1 for no-value pixels.

The data was randomly split into 5 equally sized partitions of  $\approx 22$  image-pairs to perform a 5-fold cross-validation.

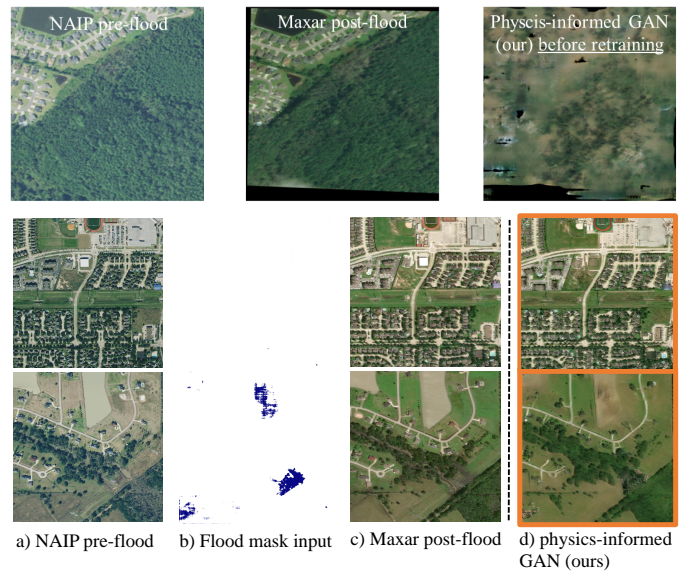


Fig. A.1: **Generalization across remote sensing instruments.**

We tested if a model can be trained on data from one remote sensing instrument and generalize to another. To do so, we trained a model on xbd2xbd and during testing changed the inputs from Maxar to NAIP imagery using naip2xbd. This experiment generated unintelligible imagery (top-row, right). This is likely due to the changes in resolution, color calibration, atmospheric noise, and more. To overcome this issue and train a model that generalizes across remote sensing instruments, we have compiled the naip2hou dataset of 5602 image-triplets (a, c in two bottom rows). A model trained and tested on this dataset generates imagery in d) that is not production ready, but suggests that a retrained model can learn to translate images across different remote sensing instruments.

#### 3) *Physics-based flood masks in xbdfathom*

We retrieve a physics-based flood mask from the hurricane Harvey flood hazard simulations of the 30m-resolution US variant of the Fathom large-scale hydraulic modeling framework; downloadable at [94]. The hindcasts for hurricane Harvey are described in [64], the US variant in [95], and the original global hydraulic model framework in [96]. The model simulates waterflow across a 2D land surface using the Venant shallow water equations and accounts for fluvial (riverine), pluvial (rainfall), and surge (coastal) flood hazards through appropriate boundary conditions.

The downloaded flood mask is a single-channel large tif for the Greater Houston area and contains the estimated flood height per  $\sim 30m/px$  pixel. We binarize the mask by thresholding values above 20 cm following the protocol in [97] which mentions that residence damages usually start to occur at this height [98]. We cut the mask into tiles that match the xbd2xbd hurricane Harvey validation set pre-flood imagery by reprojecting the flood mask onto same coordinate system, resampling the mask to  $\sim 0.5m/px$  via nearest neighbor interpolation, and then cropping out matching tiles.

#### 4) Generalization data *naip2xbd*, *naip2hou*, and *hou-seg*

We created the datasets *naip2xbd*, *naip2hou*, and *hou-seg* to test if our model can visualize flooding with inputs from the NAIP aerial imagery and targets from Maxar satellite imagery.

The *naip2xbd* imagery was compiled by sourcing one NAIP imagery tile for every post-flood tile in the *xbd2xbd* dataset that belongs to the *hv*, *fl*, *mi*, or *mw* events. To do so, we extracted the geocoordinates for every flood tile in the *xbd xvview2* dataset. The *xvview2* dataset contained erroneous geoinformation for a few tiles, which we corrected by plotting all tiles. Using the extracted bounding boxes, we downloaded the NAIP imagery tiles using Google Earth Engine’s javascript API. We upsampled the NAIP tiles from 1m/px to 0.5m/px. Further, there was distortion and an offset of 1-20m between the NAIP inputs and Maxar targets. To overcome this variance partially, we orthorectified the Maxar targets using SWIFT features, such that, both images are better aligned. In total, the dataset contains 6.1GB and 2063 HD image-triplets (1260 train, 394 test, and 409 held-out) using a random split.

The *naip2hou* and *hou-seg* contain post-flood images from a single swath of a Maxar satellite over West Houston after hurricane Katrina. The swath was sourced from Maxar’s open data repository. We hand-selected areas that contained significant flooding, tiled the imagery of those areas, and hand-labelled a subset. We hand-labelled imagery with the help of the “select regions of similar color” tool in Adobe Photoshop. After tiling the dataset, we download the associated NAIP imagery using Google Earth Engine. The *hou-seg* dataset contains 260 HD image-pairs and *naip2hou* contains 16GB of 5602 image-triplets (4481 train, 840 test, and 281 hold-out).

#### B. Pre- and post-reforestation imagery

We compiled image triplets for visualizing reforestation, as seen in Fig. A.2. To select the areas, we went through all of VERA registered ARR (Afforestation, Reforestation, and Revegetation) carbon projects until 2022, and downloaded the shapefiles (.kml or .kmz) when they were available. We used Google Earth Pro to first confirm that cloud-free high-resolution (<3m/px) imagery for the years before project start was available over the shapefile regions. Then we visually verified that reforestation actually occurred. These conditions were considered satisfied if we had imagery of bare land where we could see trees planted and grown over the years. In that case, we considered “pre-reforestation” as the earliest available imagery before we could see that trees were planted. For instance, if on the high-resolution imagery, we saw that trees were planted in 2010, then we would go back in time to the previously available imagery which could be 2009 or 2005, depending on the regions. For the “post-reforestation” imagery, we selected the most recent imagery available without clouds, so ideally it would be 2022. Our dataset timestamps go from 2005 to 2022 with some in-between years when those years were not available or not good quality (too many clouds, overlapping rasters from different years, etc).

Ultimately, the selected high-resolution images of before and after reforestation were exported from Google Earth Pro (Map data: Google, Maxar Technologies, CNS/Airbus)

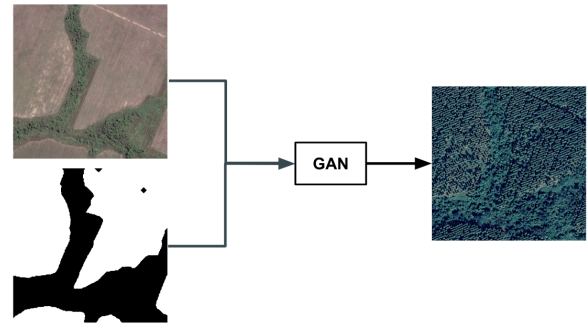


Fig. A.2: **Model Architecture for Reforestation.** Our model leverages the semantic image synthesis model, Pix2pixHD, and combines a pre-reforestation satellite image with a reforestation map to generate post-reforestation satellite imagery.



Fig. A.3: **Generated post-flooding imagery of 64 randomly chosen tiles** using high-res. flood masks from hurricanes Harvey and Florence validation set.

with a resolution of 4800x4800 and an eye altitude of 1500 meters. Our filenames follow the convention <grid reference time>\_eye\_alt\_ <eye\_altitude>m\_ <year\_aquisition>. For example, 15QVV3535563291\_eye\_alt\_1500m\_2019. The image of the pre-reforestation with the visual of the shapefile layer was also exported to be used as the binary reforested area mask. The image with the visual of the shapefile was converted to a binary mask using an image processing method that removed all non-white pixels.

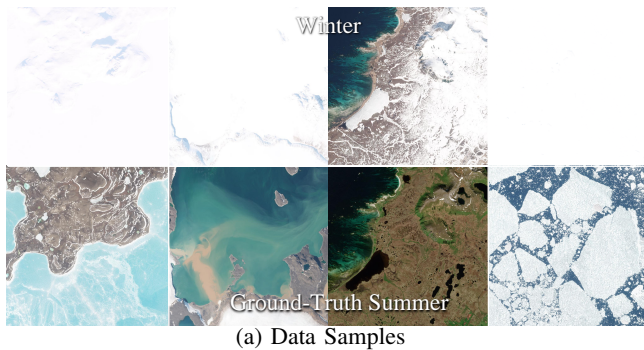
The 1024x1024 tiles were generated from the 4800x4800 exported images. The binary reforestation area masks were stacked on top of the RGB images. Only tiles that had pixels belonging to a reforested area were saved. In total, the forest dataset contains 5.5GB of 1272 image triplets (1026 train, 246 test) at a random 80/20 split across all collected regions and the forest-gtm datasets contains 460MB or 107 held-out image triplets from a previously unseen area in Guatemala.

#### C. Pre- and post-melt Arctic sea ice imagery

To visualize melting Arctic sea ice we created 19445 image-triplets of pre-melt image, post-melt image, and post-melt segmentation mask, as displayed in Fig. A.5. Because the retreat of Arctic sea ice occurs over decades, we used Winter



Fig. A.4: **Dalle-2**. We prompted the diffusion-based model, DALL-E 2, to generate ‘A realistic and physically-consistent satellite image of Houston, TX being flooded.’ The visualized urban scenery is noisy and lacks the detail of buildings (zoom in). The blur is likely due to the complexity of generating the high-frequency and structured information that characterizes satellite images. This further indicates the continued challenge that generating satellite imagery, instead of drawings or first person images, is posing to deep generative vision models.



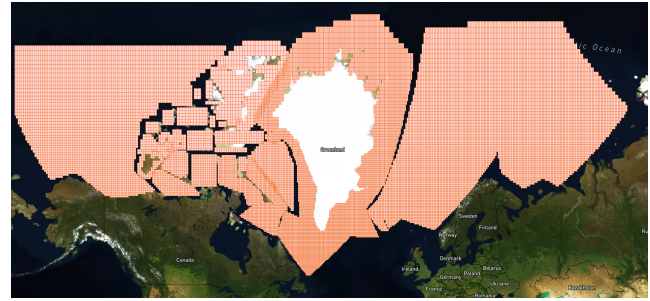
(a) Data Samples

Fig. A.5: We allow the extension of *Earth Intelligence Engine* to visualize melting Arctic sea ice by publishing an according dataset.

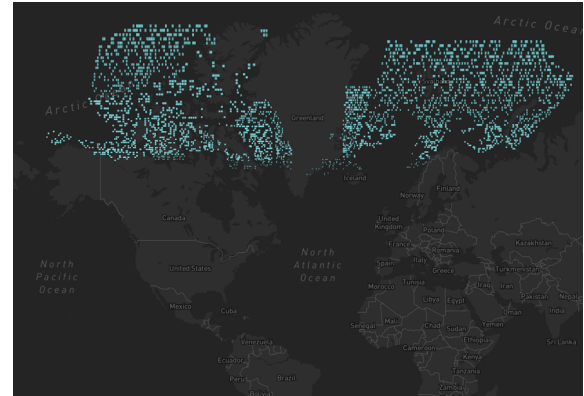
and Summer imagery as pre- and post-melt, respectively. We found  $\sim 20k$  matching pre- and post-melt images by finding matching pairs across 27172 Winter images in 1st Oct. 2019 - 1st May 2020 and 32433 Summer images in 1st Jun. - 31st Aug. 2020 within the study area in Fig. A.6a. We downloaded cloud-free Sentinel-2 MSI Level 1-C visual imagery at 10m/px resolution in tiles of 1024x1024px that matched the criteria. Our ice segmentation model creates binary ice segmentation masks (1=ice) by thresholding grayscale images into white and non-white (intensity < 255) areas,  $x = (1 \text{ if } x=1 \text{ else } 0)$ . We created the post-melt segmentation masks by applying the segmentation model on the post-melt imagery. After creating segmentation masks, we rejected all image pairs that only contain ocean or land(mask=0). Figure A.6b shows the final locations of all image pairs.

## APPENDIX B FLOOD SEGMENTATION MODEL

We evaluate the physical-consistency of the generated flood imagery by measuring intersection over union (IoU). Specif-



(a) Study Area



(b) Final data distribution

Fig. A.6: We compiled a dataset of  $\sim 20k$  image-pairs of the Arctic to visualize melting Arctic sea ice.

ically, we measure the IoU of a flood mask that is derived from the generated image via a flood segmentation model with the ground-truth flood mask that was used as input. Here, we provide additional methodology and results for the flood segmentation model.

We trained two independent flood segmentation models – one for the main xbd2xbd experiments in Section IV-B using the 109 labelled images in xbd-seg and another on the 260 labeled images in the hou-seg dataset for Section IV-D2. Our implementation is a pix2pix model [12], which differs from pix2pixHD [13] and uses a vanilla UNet as generator. We trained it from scratch to minimize a modified loss function that minimizes L1-loss and IoU in addition to adversarial loss and finetuned the last layers on L1-loss.

For both datasets, we used a UNet with 120 trainable layers to predict 1-channel segmentation masks from 3-channel images of size 1024x1024. The loss function is a weighted sum (1:1:5) of a vanilla GAN loss, L1 loss, and negative IoU wrt. the ground-truth segmentation mask. We trained the model for 80 epochs with batch size, 8, and learning rate, 0.0002, on 4 GPUs. For the xbd-seg dataset, we then fix the first 100 layers and fine-tune the last 20 layer network for 80 epochs using only L1 and IoU loss (0:1:3) and otherwise the same hyperparameters.

We experimented with decreasing the number of epochs and removing the GAN loss to train a UNet on L1+IoU, which both individually decreased performance. Otherwise, we are using the default parameters in <https://github.com/junyanz/pytorch-CycleGAN-and-pix2pix> master branch on 09/2020.

For the hou-seg dataset, we re-trained the same network from scratch on the hou-seg data and did not fine-tune the network.

The xbd-seg dataset is relatively small with 109 image-pairs. This data sounds extremely limited, but note that 109 images at HD resolution would equal 1744 image-pairs at 128x128 resolution. Nevertheless, to overcome the data limitation, we use a 5-fold cross validation as train-test split. I.e., we randomly split the dataset into 5 equally sized partitions of  $\approx 22$  image-pairs and train the model with considered hyperparameters 5-times on 4 partitions while holding out 1 partition. After finding the model with the best hyperparameters, we train it on the full labeled dataset and use it to infer flood masks on all data in xbd2xbd. The model for hou-seg was trained using a single random 80-20 train-test split and otherwise same hyperparameters as for xbd-seg.

The model on the xbd-seg dataset has IoU 0.343 and on the hou-seg has IoU 0.23. Many images in our dataset display very little flooding and, hence, achieving high IoU scores is very difficult. The IoU of 0.343 matches expectations of the pix2pix model [12]. For a better understanding that the IoU of 0.23 on hou-seg should be sufficient, we are plotting 20 randomly selected samples from the hou-seg test set in Fig. D.8.

Future work, could likely improve the IoU by choosing a network backbone that is pretrained on visual satellite imagery, more complex segmentation models [99], or increasing the data size.

The segmentation model could be improved, e.g., by considering more novel segmentation architectures, such as, PSP-Net [100], PAN [101], or DeepLabv3+[102]. Due to the limited amount of data, we expect semi-supervised learning approaches to impact the performance more than architectural choices. Thus, we experimented with networks that were pretrained on ImageNet, but they classified "background" for every image, which led us to believe that mid-to-late-stage layers have little to no signal and only early layers would be useful. Future work, could use networks that are pretrained via contrastive or reconstruction loss on other remote sensing tasks and datasets, similar to [103], [104].

## APPENDIX C EXPERIMENTS

### A. Data Augmentation.

To visualize floods, we applied standard data augmentation, here rotation, random cropping, hue, and contrast variation, and state-of-the art augmentation - here elastic transformations [105]. Furthermore, spectral normalization [106] was used to stabilize the training of the discriminator. A relativistic loss function has been implemented to stabilize adversarial training. We also experimented with training pix2pixHD on LPIPS loss. Quantitative evaluation of these experiments, however, showed that they did not have significant impact on the performance and, ultimately, the results in the paper have been generated by the pytorch implementation of pix2pixHD [13] extended to 4-channel inputs.

To visualize reforestation, we used downscale (to 0.8 scale), h- and v-flip, and colorjitter (brightness=0.4, contrast=0.2, saturation=0, hue=0) augmentations with  $p = 0.67$  from the

albumations library [107]. The model hyperparameters are chosen to equal the pytorch implementation in [13].

### B. Pre-training LPIPS on satellite imagery.

The standard LPIPS did not clearly distinguish in between the handcrafted baseline and the physics-informed GAN, contrasting the opinion of a human evaluator. This is most likely because LPIPS currently leverages a neural network that was trained on object classification from ImageNet. The neural network might not be capable to extract meaningful high-level features to compare the similarity of satellite images. In preliminary tests, we ran inference using an ImageNet-pretrained network and saw that it classified all satellite imagery as background image, indicating that the network did not learn features to distinguish satellite images from each other. Future work, will use LPIPS with a network trained to have satellite imagery specific features, e.g., Tile2Vec or a land-use segmentation [108] model.

## APPENDIX D RESULTS

Figure D.7 shows inputs, targets, and predictions from the xbd2xbd and xbdFathom dataset. The two top rows show selected success cases. The model accurately in-paints a brown-colored flood (3rd and 5th col.) in the areas of the xbd2xbd (2nd col.) and xbdFathom (6th col.) flood masks. Many high-resolution features, such as the location of the houses, trees, or roads seem to be maintained across pre-flood (1st col.) and generated image (3rd and 5th col.); matching the expectations from the xbd2xbd target imagery (4th col.). In many locations within the images, the model seems to correctly visualize a flood height that is lower than house roofs or forest canopy (except for, e.g., top-left area in 5th col., 2nd row).

The next five rows show imagery that is randomly selected from the xbd2xbd test dataset. Overall, there does not seem to be a substantial difference in quality in between the visualizations of the xbd2xbd observation-derived (2nd col.) or xbdFathom physics-based (6th col.) flood masks. Similar to the success cases, the model seems to maintain the location of many houses in residential areas, but also overpaints structure occasionally with a flood-brown (e.g., 5th col., 3rd row, bottom-left area). The model seems to ignore masks that contain floods in every pixel (e.g., 5th col., 6th row), which possibly suggests that learned weights are only activated by spatial gradients in the flood mask.

The two bottom rows show failure cases: The penultimate row indicates that the model fails to capture high-rise buildings, cars, or bridges, which are features that occur rarely in the training dataset. The last row shows that the low-res. flood masks in xbd2xbd can contain partially inaccurate labels, in this case missing the standing flood in the forested area (comparing 2nd to 4th col.). The last row also shows a failure case where the model visualizes an unnatural flood color with many distortions (5th col.).

We attach an additional 20 randomly chosen prediction from the naip2hou dataset in Fig. D.8 to illustrate the performance of the naip2hou flood segmentation model. Each image triplet

shows the input image (left), prediction (middle), and ground-truth (right). The mean IoU of our model over the validation dataset is 0.23, which is below average performance of a segmentation model. But, note that the IoU for images with significant flooding is generally  $> 0.4$  and the IoU for images with near-zero water is 0.0 (e.g., in the 2nd to bottom row). The images with near-zero flooding skew the reported average IoU towards 0.

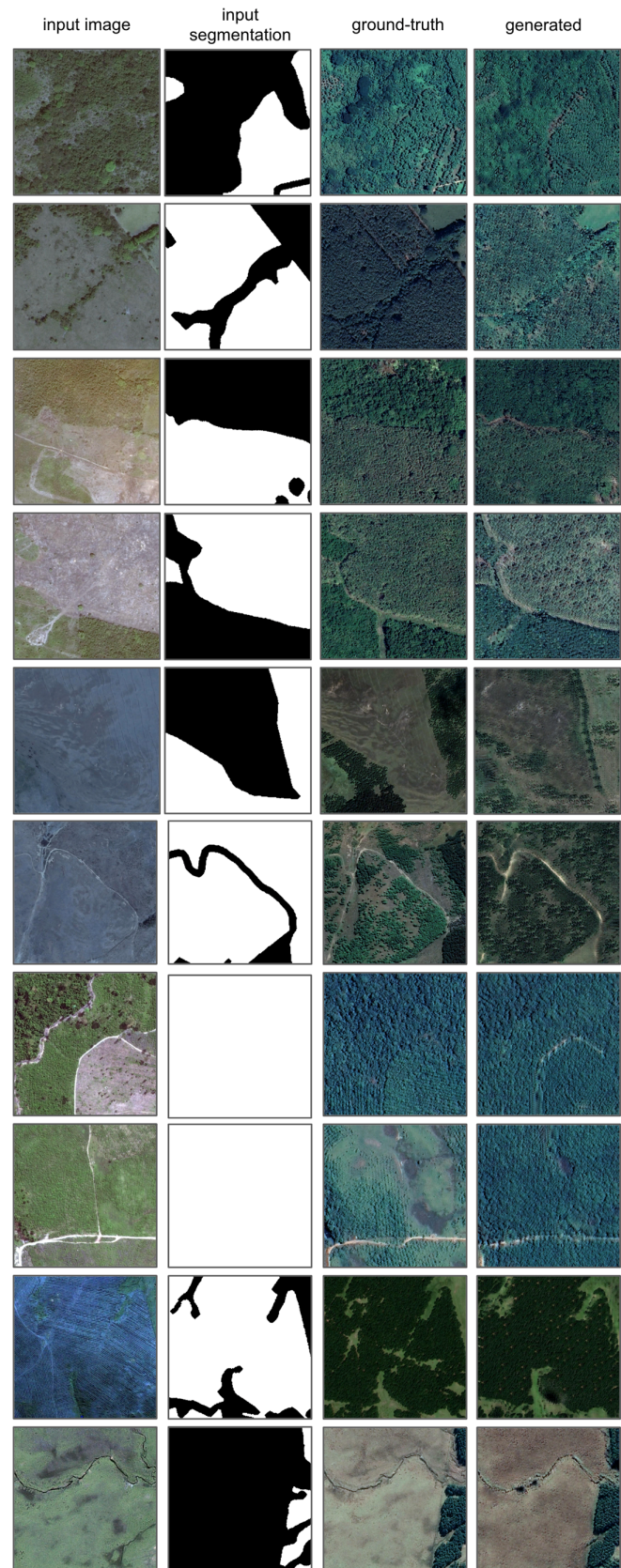


Fig. D.9: Generated visualizations for 10 randomly chosen tiles of the **forest** validation dataset. The white areas in the input segmentation indicates areas in the ground-truth image that have been reforested after the input image was taken.

We also plot 10 randomly chosen images from the forest validation dataset in Fig. D.9.



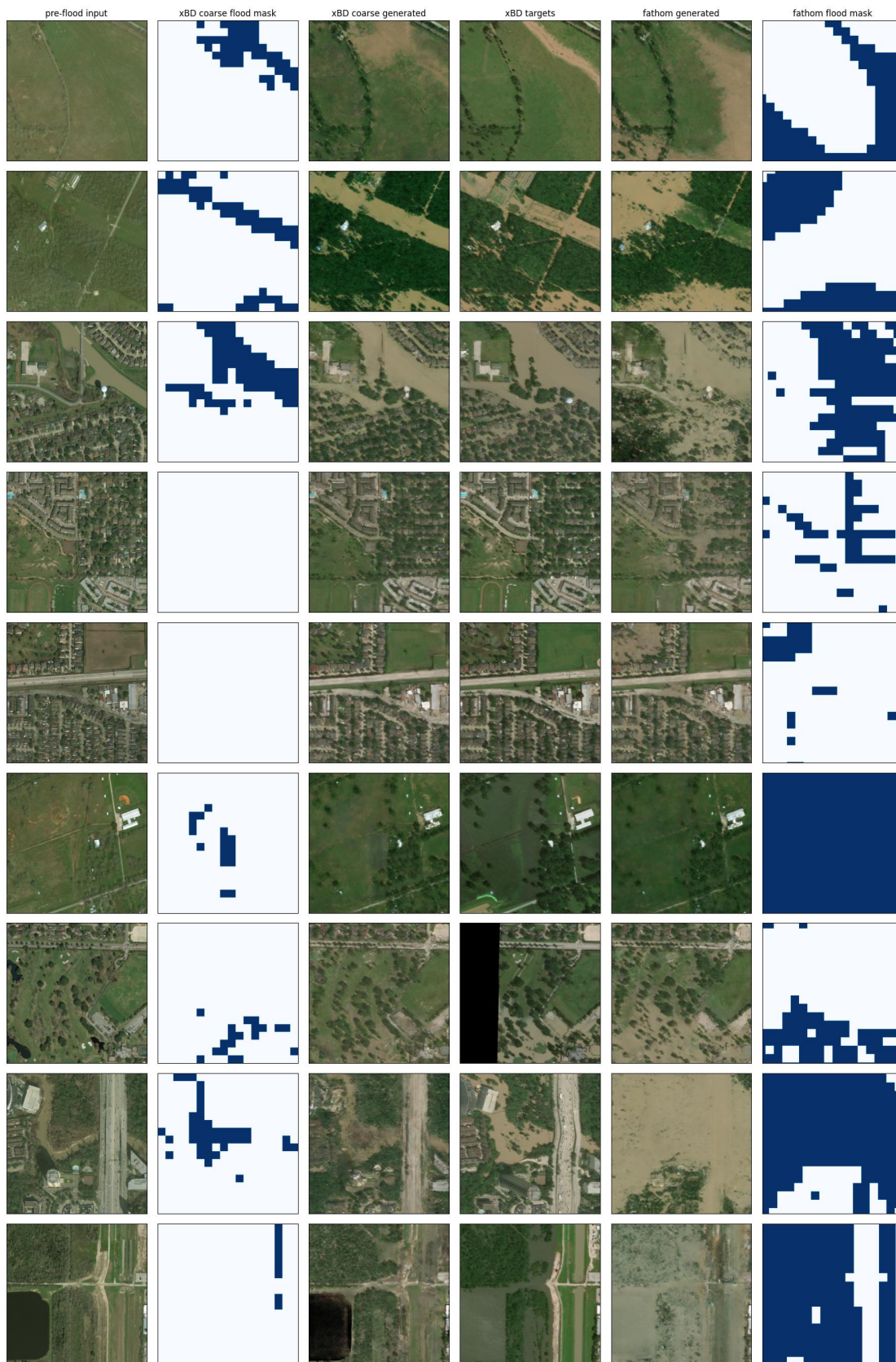


Fig. D.7: The plot shows inputs, targets, and predictions from the xbd2xbd hurricane Harvey validation set (1st-4th col.) and the xbd fathom dataset (5th-6th. col.). The selected imagery in the first two rows displays how differing flood mask inputs (2nd and 6th col.) affect the generated visualization (3rd and 5th col.) if the pre-flood input image (1st col.) and model are held fixed. The next five rows are randomly selected and the last two rows display selected failure cases.

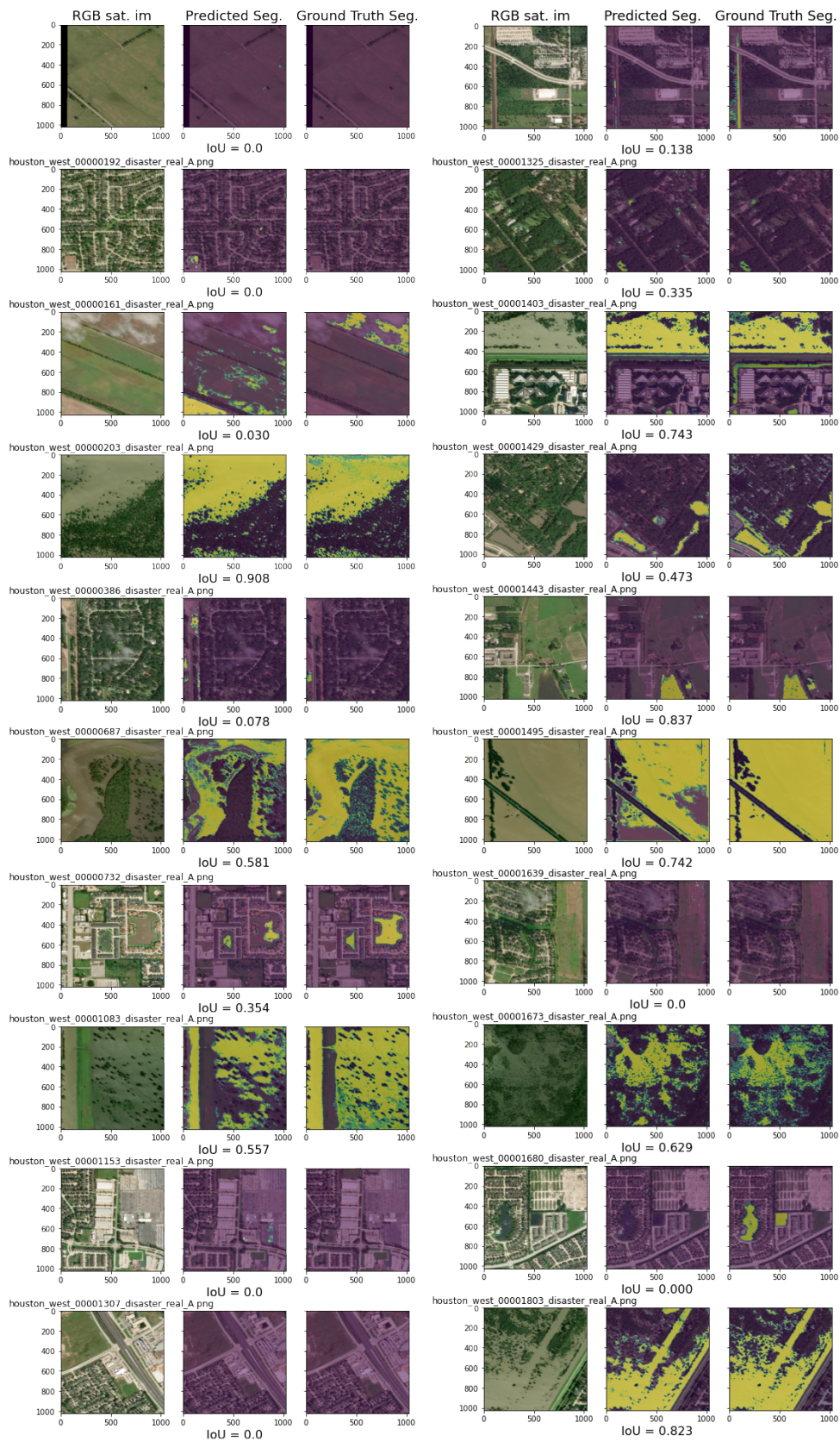


Fig. D.8: Generated segmentation masks for 20 randomly chosen tiles of naip2hou dataset (zoom in). The average IoU across the dataset is 0.23.